scientific reports

Check for updates

OPEN

Performance comparison of CTAB-modified NiO, ZnO, and SnO_2 sensors for CO and CH_4 detection in environmental and health applications

Poundoss Chellamuthu[1], Kirubaveni Savarimuthu[2], R. Krishnamoorthy[3], T. Yuvaraj[1], Mohit Bajaj[4,5,7] & Oleksandr Rubanenko[6]✉

In industrial and environmental monitoring, high-sensitivity and response-time sensors are a major challenge. In this research, ZnO, NiO, and SnO_2 nanostructures were prepared via a Surfactant (CTAB)-assisted hydrothermal process. Surfactant improves surface activity and porosity for controlled development. A stable p–n heterojunction was formed by including PEDOT: PSS in n-type oxides. The fabricated sensors were put through an intensive testing procedure for the detection of CO and CH_4 at ambient temperature (30 °C) and at different concentrations (2–10 ppm). The maximum sensitivity of the PEDOT: PSS/SnO_2 heterojunction was 92.3% for CO and 90.8% for CH_4. Its response and recovery times were 10/5 s and 15/8 s, respectively. The developed sensors exhibited a linear response pattern and excellent repeatability across a 24-h evaluation, with five testing cycles of 250 s each. Characterization of structural and surface properties (XRD, EDS, BET, UV, JV, and EIS) confirmed that high crystallinity, nanoscale structure, and enhanced surface area were responsible for enhanced sensing performance. Based on the results, PEDOT: PSS heterojunction assembly combined with CTAB-assisted hydrothermal synthesis may be employed to synthesize high-performance, low-cost gas sensors for real-time detection of harmful and inflammable gases.

Keywords Hydrothermal synthesis, Metal oxides, Surfactant, Heterojunction, Response/recovery times, Sensitivity

The increasing emissions of toxic gases like carbon monoxide (CO) and methane (CH_4) from household sources, vehicle exhaust, and industrial operations are a severe threat to human health and the environment[1]. The most highly flammable greenhouse gas, CH_4, is the main cause of global warming, while CO is a colorless, odorless gas that reacts strongly with hemoglobin to alter oxygen delivery in the human body[2]. Thus, the development of high-fidelity, efficient, and accurate gas sensors is of high importance for environmental monitoring and safety management[3]. Nanomaterials are increasingly regarded as advanced materials because their distinctive physicochemical, structural, and functional characteristics support transformative applications across energy, biomedicine, food science, and environmental technologies, while simultaneously enabling highly effective sensing of environmental pollutants, biomedical markers, humidity variations, hazardous gases, and explosive substances[4]. Metal oxide semiconductors (MOS) remain at the forefront of gas sensor technology because of their promising composition of high sensitivity, high stability, and low cost. These MOS materials, such as zinc oxide (ZnO), nickel oxide (NiO), and tin oxide (SnO_2), continue to be in-depth researched. Their room-temperature operation capabilities with their broad band gaps, their tunable morphologies that provide accurate control of active sites, and the creation of novel, simple synthesis processes, which heighten their sensing

[1]Centre for Smart Energy Systems, Chennai Institute of Technology, Chennai 600069, India. [2]Department of Electronics and Communication Engineering, College of Engineering, Anna University, Guindy, Chennai 600025, India. [3]Centre for Advanced Wireless Integrated Technology, Chennai Institute of Technology, Chennai 600069, India. [4]Department of Electrical Engineering, Graphic Era (Deemed to be University), Dehradun 248002, India. [5]Hourani Center for Applied Scientific Research, Al-Ahliyya Amman University, Amman, Jordan. [6]Department of Power Plants and System, Vinnytsia National Technical University, Vinnytsia 21000, Ukraine. [7] College of Engineering, University of Business and Technology, Jeddah 21448, Saudi Arabia. ✉email: rubanenko.o.y@vntu.edu.ua

ability, are the reasons why they are being given much attention[5–7]. SnO_2 is one of the most favored n-type semiconductors with a vast potential for CO and CH_4 sensing. Its high electron mobility as well as excellent gas adsorption properties are the key reasons behind this performance[8]. In a similar manner, ZnO also responds sensitively to reducing gases because it has a high surface-to-volume ratio as well as oxygen vacancy availability[9]. Conversely, the p-type semiconductor NiO is well known for enhancing sensor selectivity and for its role in the creation of efficient p-n heterojunctions with n-type metal oxides[7]. Recent studies illustrate that surfactants, for example, cetyltrimethylammonium bromide (CTAB), can efficiently modify the active sites, porosity, and surface morphology of nanostructured materials during synthesis, enhancing their gas sensing capacity[10]. In addition, hybridization of conducting polymers with metal oxides, e.g., poly (3,4-ethylenedioxythiophene) polystyrene sulfonate (PEDOT: PSS), is a promising method to fabricate p–n heterojunctions, reduce response/recovery times, and improve sensitivity through improved charge transfer properties[11,12]. Heterojunction-based nanostructures are increasingly important in sensing research because the interfacial charge separation they provide significantly enhances sensitivity, selectivity, and overall gas-sensing performance[13]. The hydrothermal process is extremely beneficial in fabricating such nanostructures owing to its straightforwardness of use, low temperature processing, and capability to produce highly crystalline material with controlled morphologies[14]. Hydrothermally synthesized MOS nanostructures for gas sensing were reported in several studies; for instance, Abbas et al.[15] employed ZnO nanorods and Sharma, K.K et al.[16] synthesized a nanostructured cubic phase SnO_2 to illustrate enhanced CO sensing, and Jaiswal et al.[17] employed SnO_2 nanosheets to realize higher CO_2 reduction. The amount of work comparing ZnO, NiO, and SnO_2 gas-sensing performance synthesized with identical conditions but involving CTAB-directed growth and PEDOT: PSS incorporation is limited. This study explores the CO and CH_4 gas sensing capability of ZnO, NiO, and SnO_2 nanostructures grown using a CTAB-mediated hydrothermal process. Surfactant-directed growth influence on morphology and role of PEDOT: PSS in constructing heterojunctions with these oxides are explored systematically. Based on a comparative study of the three materials, the most suitable candidate for the detection of CO and CH_4 is presented, which is useful when designing high-performance gas sensors.

Literature review of metal oxide nanostructures for CO and CH_4 gas sensing

With emphasis on the detection of CO and CH_4, Table 1 presents an overview of the latest work on the gas sensing capability of hydrothermally synthesized metal oxides, situating the present work within its context. It gives prominence to important factors such as operating temperature, gas sensing response, composition, and structure.

Research gap and study contribution

The potential of materials like PEDOT: PSS, CTAB, and metal oxides to enhance electrical conductivity and sensing capability is highlighted by recent developments in nanocomposite-based gas sensors. Nevertheless, little is known about how these elements can work together, such as when PEDOT: PSS layers are combined with CTAB–SnO_2/ZnO heterostructures. While industrial gases like carbon monoxide (CO) and methane (CH_4) have received little attention, the majority of published investigations focus on particular metal oxides that target volatile organic compounds (VOCs) or humidity detection. Furthermore, several high-performing designs use expensive or complicated materials (such as MXenes), which makes it harder to fabricate sensors on a large scale at a reasonable cost. In order to overcome these constraints, the current work prepares ZnO, NiO, and SnO_2 nanostructures using CTAB-assisted hydrothermal synthesis in identical conditions, ensuring a direct comparison of their gas-sensing capabilities. By forming p–n heterojunctions through integration with the p-type conductive polymer PEDOT: PSS, response and recovery times are accelerated, operating

Method	Materials/system	Key findings	Limitations	Research gap	Ref.
Chemical synthesis routes (hydrothermal, sol–gel, CVD)	1D oxide nanostructures (ZnO, SnO_2, TiO_2, etc.)	Discussed control over morphology and crystallinity through different synthesis methods	Did not explore polymer or surfactant-assisted synthesis effects	Need to evaluate surfactant-assisted 1D nanostructures (e.g., CTAB) for improved sensing performance	[18] 2019
Inkjet printing and sol–gel synthesis	PEDOT: PSS/ZnO paper-based hydrazine sensor	Demonstrated high flexibility, cost-effectiveness, and good sensitivity for hydrazine detection at room temperature	Limited to liquid-phase sensing; lacks humidity or gas sensing exploration	Integration of PEDOT: PSS/ZnO heterostructures for real-time gas or humidity sensing not yet studied	[19] 2020
Review of electroactive hybrid nanocomposites	Organic–inorganic nanocomposites using nanostructured materials	Highlighted enhanced gas sensing due to improved charge mobility and structural porosity	Lacks experimental validation and detailed comparison of hybrid vs. pure oxide sensors	Experimental correlation between morphology, sensitivity, and humidity response remains limited	[20] 2022
Hydrothermal method and surface modification	Au-modified SnO_2/ZnO composite	Achieved high CO gas sensitivity at room temperature due to Au catalytic activity and SnO_2/ZnO heterojunction	Performance analyzed for a single gas; lacks humidity interference study	Study of multi-gas selectivity and humidity effect on SnO_2/ZnO heterostructure is still required	[21] 2025
Review of heterojunction photocatalysts	Bi-based S/Z heterojunctions	Reviewed Bi-based S/Z-scheme catalysts with efficient charge migration for key photocatalytic reactions.	Provides a solid photocatalytic foundation, opening space to explore S/Z heterojunctions for gas-sensing applications	Need to evaluate S/Z-scheme heterojunctions for enhancing charge separation and gas-sensing behavior	[22] 2025
Review of synthesis and characterization techniques	Metal oxide–polymer hybrid composites	Summarized advances in synthesis and multifunctional applications such as sensing, energy storage, and catalysis	Review focused more on synthesis than on interfacial charge transfer mechanisms	Need to investigate synergistic effects between polymers and metal oxides for enhanced sensing selectivity	[23] 2025

Table 1. Recent literature on CTAB-assisted metal oxides and PEDOT: PSS for gas sensing.

temperatures are decreased, and charge transfer is improved. This study simultaneously fills important gaps in dual gas detection (CO and CH_4), morphology-controlled synthesis, and practical p–n heterojunction design by methodically examining all three oxides in a single experimental environment. The method offers a scalable and economic path to high-performance gas sensors appropriate for industrial safety and environmental monitoring applications.

Materials and methods

Materials

The synthesis of oxide nanostructures was carried out using high-purity metal precursors such as tin(IV) chloride pentahydrate ($SnCl_4{\cdot}5\ H_2O$), zinc nitrate hexahydrate ($Zn(NO_3)_2{\cdot}6\ H_2O$), and nickel nitrate hexahydrate ($Ni(NO_3)_2{\cdot}6\ H_2O$). In order to control the shape and surface properties of nanoparticles, CTAB acted as a surfactant. A p-type conducting polymer (PEDOT: PSS) was chosen because of its p-type conductivity and its ability to create a p–n heterojunction with SnO_2, ZnO, and NiO, increasing the charge separation at this interface and enhancing the electrical response of the sensor for reducing gases. All compounds were utilized just as originally provided, requiring no additional purification. Both the synthesis and post-treatment processes employed ethanol and deionized water as solvents.

Synthesis of CTAB-assisted metal oxide nanostructures

ZnO, NiO, and SnO_2 were all individually synthesized by a hydrothermal process[24] with CTAB added to change shape and enhance surface activity. For each oxide, the surfactant-assisted precursor solution was made by dissolving 2 moles of CTAB in 80 milliliters of deionized water. Next, the addition of the appropriate metal precursor: tin(IV) chloride for SnO_2, nickel nitrate for NiO, and zinc nitrate for ZnO. For four hours, the solutions were kept at 90 °C to facilitate the nucleation and growth of nanostructures in Teflon-lined stainless-steel autoclaves. The precipitates were extracted by centrifugation, repeatedly washed with ethanol and deionized water, and then dried at 60 °C after cooling to ambient temperature. Then, as shown in Fig. 1, calcination was carried out at 400 °C to improve phase purity and crystallinity. Each oxide was prepared in the same procedure, ensuring a controlled comparison of surface properties, morphology, and ensuing gas-sensing ability. ZnO, NiO, and SnO_2 nanostructures were produced using the synthesis conditions shown in Table 2.

Integration with PEDOT: PSS

To improve charge transport and sensor response, PEDOT: PSS was applied to the individual metal oxide powders (paste) to create p–n heterojunctions. Acetone, ethanol, and deionized water were used to clean fluorine-doped tin oxide (FTO) glass substrates, which were then dried under nitrogen. To increase adhesion and electrical conductivity, PEDOT: PSS was spin-coated[25] onto the oxide layer for 60 s at 3000 rpm, and then annealed for 30 min at 120 °C, as illustrated in Fig. 2. Effective electron–hole separation and improved gas-sensing performance were made possible by this process, which ensured consistent polymer coverage over the nanostructured oxide surfaces.

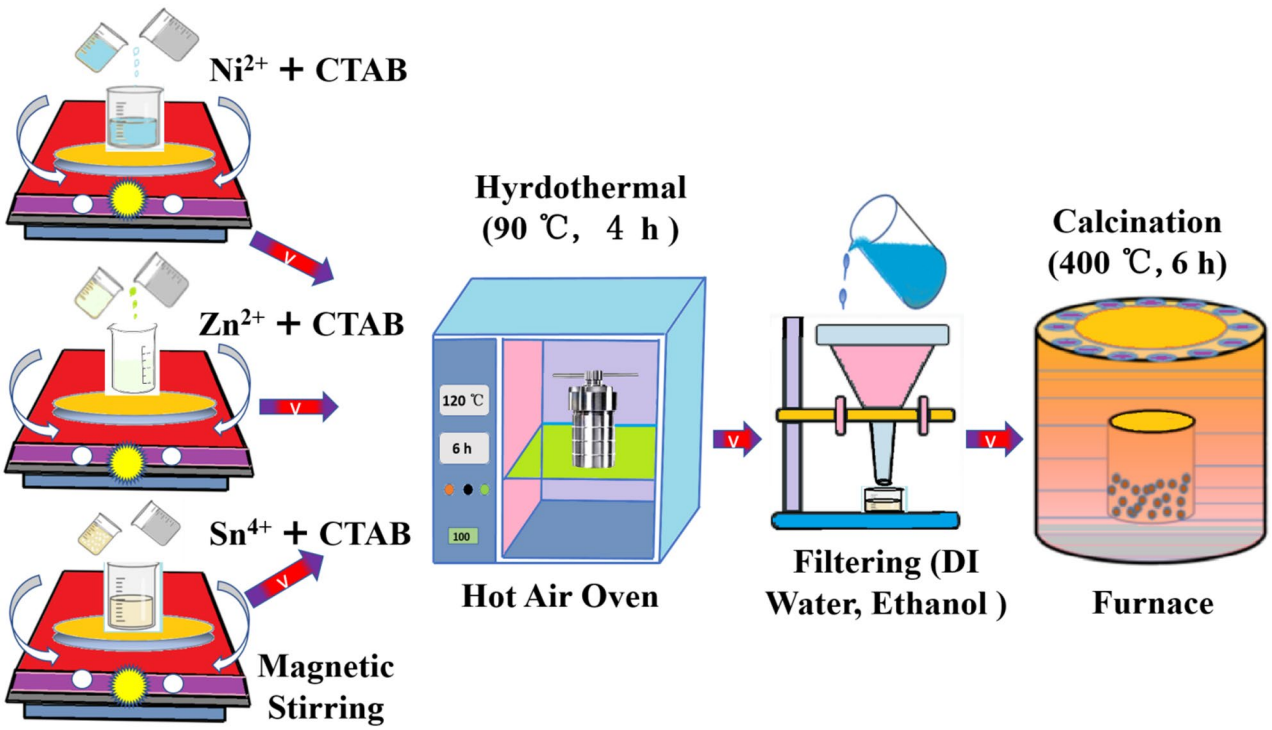

Fig. 1. Schematic illustration of the synthesis methods used for SnO_2, ZnO, and NiO nanomaterials.

Material	CTAB (moles)	Temperature (°C)	Time (h)	Solvent volume (mL)
ZnO	2	90	4	80
NiO	2	90	4	80
SnO_2	2	90	4	80

Table 2. Synthesis parameters of metal oxide nanostructures.

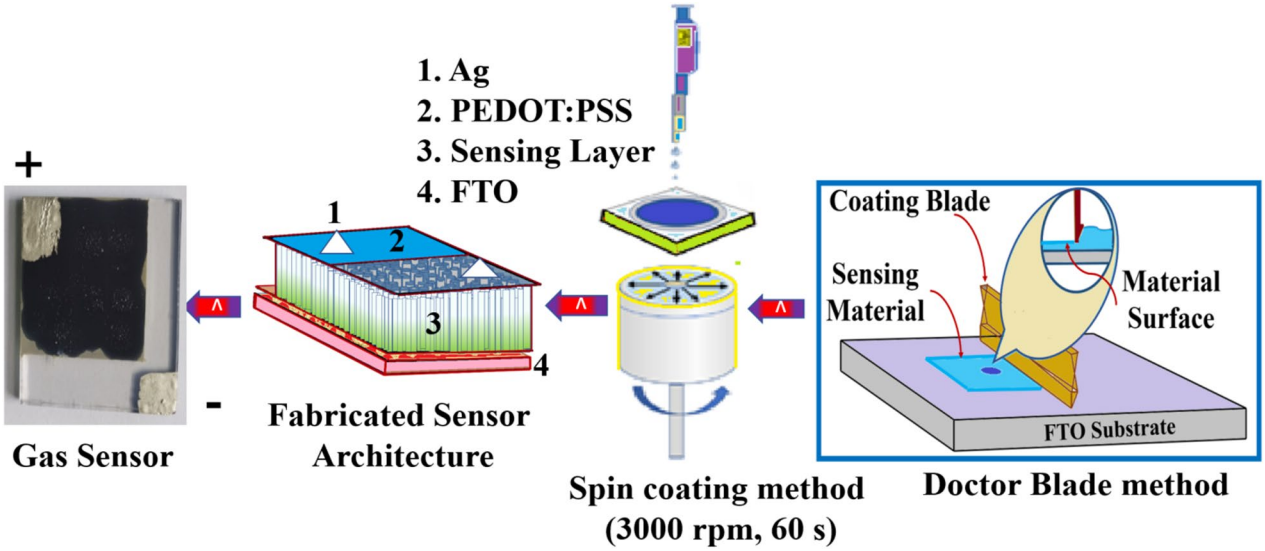

Fig. 2. Fabrication of the sensor device showing the layer-by-layer structure made up of the FTO substrate, Ag, PEDOT: PSS, and sensing layer.

Material characterizations

The synthesized nanostructures have been comprehensively characterized in terms of their morphological, structural, and chemical characteristics. X-ray diffraction (XRD) was used to determine the phase purity and crystal structure. The size, shape, and surface characteristics of the particles were revealed using field-emission scanning electron microscopy (FESEM analysis). Elemental composition and oxidation states were verified by energy-dispersive X-ray spectroscopy (EDS). Brunauer–Emmett–Teller (BET) surface area analysis was performed for measuring the specific surface area and porosity. The optical band gap of the synthesized materials was estimated through UV–Vis analysis, which gives valuable information concerning their electrical properties and photon interaction efficiency. The nature of electrical transport in terms of charge carrier dynamics and junction behavior was analyzed through current–voltage (J–V) measurements. The interfacial charge transfer resistance and electrical concepts affecting the gas sensing mechanism have been established using electrochemical impedance spectroscopy (EIS). In addition, these methods establish insight into how the chemical and physical characteristics of each oxide were affected by CTAB-assisted hydrothermal synthesis and thus had an effect on the performance of gas sensors.

XRD

The crystalline structure and phase purity of the synthesized NiO[26], ZnO[27], and SnO_2[28] nanoparticles were calculated by XRD analysis, and the findings are shown in Fig. 3a–c. A face-centered cubic structure was established by the characteristic peaks in the diffraction pattern of the NiO sample (JCPDS Card No. 47-1049). All of the ZnO nanoparticles' diffraction peaks were consistent with the standard reference (JCPDS Card No. 36-1451) with no deviation, which meant they had a hexagonal wurtzite structure. Based on the reference data from JCPDS Card No. 41-1445, the pattern observed for the SnO_2 sample confirmed a tetragonal rutile structure.

The high phase purity of the synthesized metal oxides was validated in every instance by the absence of unwanted diffraction peaks, confirming the effectiveness of the adopted synthesis process in producing phase-pure nanomaterials for further gas sensing investigation. For the synthesis of ZnO, NiO, and SnO_2, the same high concentration of CTAB was used to develop a consistent, structure-directing environment. However, the completely distinct crystallographic properties that were revealed by XRD, where ZnO formed large, well-defined crystallites, NiO exhibited intermediate characteristics, and SnO_2 formed the smallest, most defect-rich nanocrystals, indicate that the effectiveness of CTAB is not universal and is instead mainly controlled by the particular composition of the metal oxide precursor. On the other hand, the growth of ZnO was less restricted by the CTAB surfactant, favoring thermodynamic crystal growth and producing a more perfect, stable lattice. This suggests that SnO_2 nucleation and growth were best regulated by the CTAB surfactant under these conditions,

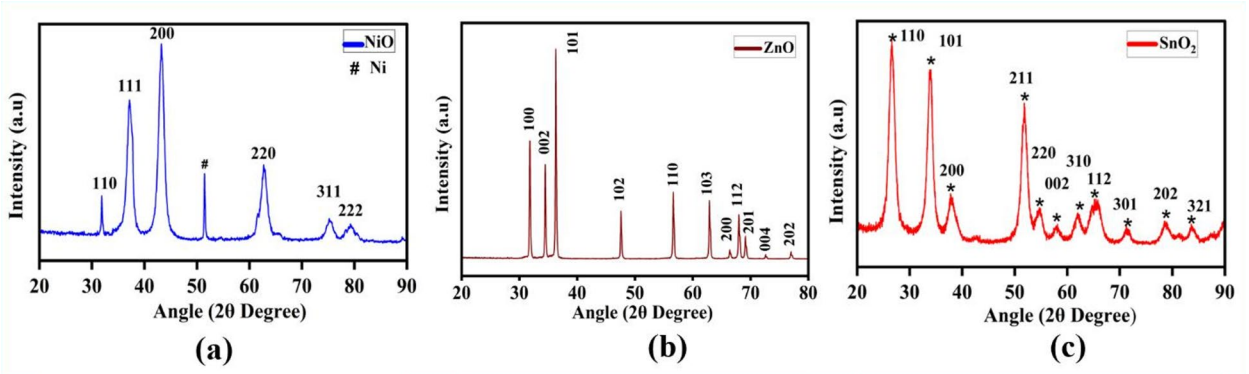

Fig. 3. XRD patterns of the synthesized nanostructures of (**a**) NiO, (**b**) ZnO, and (**c**) SnO_2.

Material	Miller indices (h, k, l)	(2θ)	(θ) in radians	FWHM (β)	(β) in radians	d-Spacing (Å)	Crystallite size (D in nm)	Micro-strain (ε)	Dislocation density (δ) nm^{-2}
NiO	3 0 0	43.2	0.377	1.281	0.022	0.017	4.43	0.013	0.051
ZnO	1 0 1	36.3	0.316	0.211	0.003	0.028	29.8	0.002	0.001
SnO_2	1 1 0	26.6	0.232	1.397	0.024	0.018	2.36	0.025	0.185

Table 3. XRD crystallite sizes calculated from Sherrer's equation.

resulting in a high defect density perfect for gas adsorption. X-ray diffraction peak broadening was used to examine the synthesized samples' crystallite size and lattice flaws. The Debye–Scherrer formula (1)[29] was used to calculate the average crystallite size (D).

$$D = \frac{k\lambda}{\beta \ cos\theta} \tag{1}$$

where λ is the X-ray wavelength (Cu Kα = 0.154 nm), β is the full width at half maximum (FWHM) of the diffraction peak in radians, θ is the Bragg angle, and k is the Scherrer constant (0.9)[30] (2) was used to estimate the microstrain (ε) caused in the powders.

$$\varepsilon = \left(\frac{\beta}{4tan\theta} \right) \tag{2}$$

In addition, using Eq. (3), the dislocation density (δ), which is the length of dislocation lines per unit volume, was calculated. Table 3 summarizes the determined values of D, ε, and δ for the NiO, ZnO, and SnO_2 samples.

$$\delta = \frac{1}{D^2} \tag{3}$$

From Table 3, it can be observed that the X-ray diffraction investigation shows a basic relationship between the three materials' defect density and crystallinity. With the largest crystallites (29.8 nm), lowest micro-strain (0.002), and least dislocation density (0.001 nm^{-2}), ZnO exhibits a highly ordered crystalline structure that should provide both exceptional operational stability and repeatability. A very defective lattice is indicated by SnO_2, which has the smallest crystallite size (2.36 nm), highest micro-strain (0.025), and maximum dislocation density (0.185 nm^{-2}). Since SnO_2 is nanostructured and defect-rich, it has a large surface area and many active sites, which makes it very promising for high-sensitivity gas detection.

NiO has values in the middle, indicating a profile that strikes a compromise between stability and sensitivity. Therefore, ZnO's high crystalline quality supports durable and dependable sensing the entire time, while SnO_2 is projected to be the most sensitive material, although its performance may be compromised by long-term instability.

FESEM analysis

FESEM was used to examine the surface morphology of the CTAB mixed NiO nanostructure, as illustrated in Fig. 4a. Aggregated nanoparticles with irregular spherical to polyhedral forms are obvious in the photograph. With both smaller nanoparticles decorating the surfaces of bigger grains, the particles' size distribution is not uniform, suggesting that CTAB functions as a surfactant to regulate nucleation and growth. The closely linked grains of NiO particles, as seen in the micrograph, can improve charge transport characteristics and the surface-to-volume ratio. The existence of bigger agglomerates and finer nanoparticles indicates that CTAB effectively

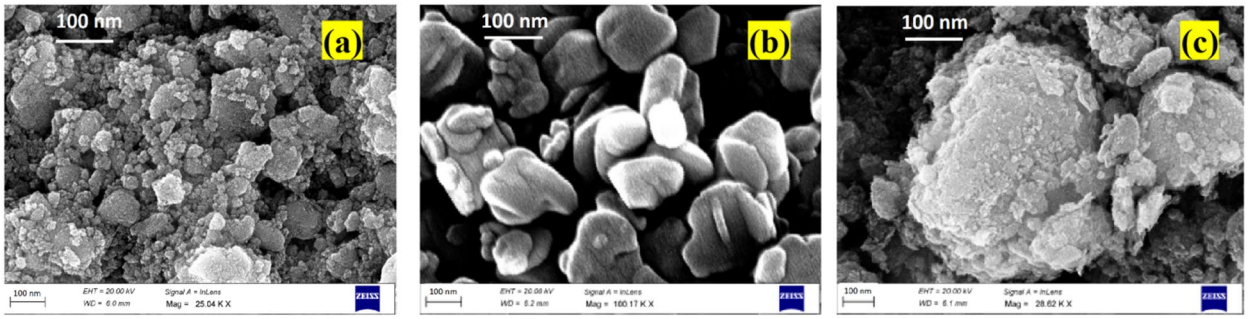

Fig. 4. FESEM images of the as-synthesized nanostructures of (**a**) NiO, (**b**) ZnO, and (**c**) SnO_2.

Material	Observed morphology (from FESEM)	Gas sensing advantages	Limitations	Overall potential	Ref.
NiO	Aggregated nanoparticles with hierarchical rough/porous surfaces	High surface area, more adsorption sites, enhanced sensitivity (due to CTAB surfactant effect)	Agglomeration may block inner surfaces, slower recovery if pores are not open	Very good for high sensitivity	32
ZnO	Well-defined, uniform hexagonal grains, smooth surfaces	Good crystallinity, stable electrical response, fast charge transport	Lower surface area, fewer active sites for adsorption	Good for stability and reproducibility	33
SnO_2	Large agglomerates composed of fine nanoparticles with rough texture	Many adsorption sites, porous multi-scale structure, high gas diffusion	Inner pores may be inaccessible if too densely packed	Excellent for high sensitivity and gas diffusion	34

Table 4. Comparison of CTAB-NiO, ZnO, and SnO_2 morphologies and gas sensing potential.

increased the synthesis-related reduction in particle size, which enhanced dispersion. Because it offers more active sites for the adsorption and desorption of analyte molecules, this structured shape is beneficial for gas sensing applications. Furthermore, the rough surface structure and porous nature seen in the FESEM image suggest the possibility of improved contact with the environment, which is very desirable in catalytic and sensing applications. These morphological characteristics, which affect the overall microstructural architecture of NiO as well as the grain connectivity, validate the effective integration of CTAB during synthesis.

The FESEM image of ZnO[31] (Fig. 4b) shows unique rod-like and hexagonal grains. The grains are more regular in size, smooth, and possess distinct boundaries. The above image illustrates the controlled crystallization of ZnO upon synthesis. The larger grains adhere to each other to create a close and dense structure. Above the surface, the structure might enable efficient charge transfer. Regular particle size distribution enables a reproducible sensing response. Smooth surfaces deliver stability, whereas edges offer reactive adsorption sites. Taking everything into consideration, the FESEM verifies the formation of crystalline ZnO structures. The FESEM image of SnO_2 (Fig. 4c) shows huge, rough-surfaced agglomerated clusters. An individual cluster consists of strongly agglomerated smaller nanoparticles. Irregular morphology suggests fast nucleation followed by clustering. Roughness of the surface gives a large number of active sites for interaction. A close-packed structure guarantees the mechanical stability of the material. The surface is fine-grained, implying multi-scale particle formation. The shape promotes adsorption and desorption during sensing processes. SnO_2 has an agglomerated, porous structure that is typically beneficial for gas sensing. With emphasis on the role of surface topology in influencing sensing behavior, Table 4 presents the morphology features of NiO, ZnO, and SnO_2 nanostructures as evaluated by FESEM analysis, along with the individual gases' sensing merits, demerits, and full potential of each material.

Morphological and elemental distribution analysis

In Figs. 5, 6 and 7, morphological and elemental distributions of three various metal oxides-NiO, ZnO, and SnO_2-are visualized using electron microscopy (EM) and elemental distribution studies. The NiO particles' morphology at a 2 µm scale is illustrated in the EM micrograph (panel a) of NiO in Fig. 5, showing a uniform distribution with grain structures of an irregular shape. Nickel presence is evidenced by the green areas in panel b of the EDS stacked image. Oxygen distribution is depicted in the O Kα1 image (panel d), while the nickel is uniformly distributed across the sample, as evidenced by the Ni Kα1 X-ray map (panel c). The Cl Kα1 X-ray map (panel e) reveals the lack of chlorine, proving the high purity of the NiO sample.

ZnO particles are particulate in shape, having clear outlines at a size of 500 nm, as in (Panel a) Fig. 6. Panel b, the EDS layered image, displays the distribution of zinc in green with minimal overlap with other elements. Panel c of the Zn Kα1 X-ray map confirms the even distribution of zinc, while panel d of the O Kα1 map shows the even distribution of oxygen throughout the sample. Similar to the NiO sample, the Cl Kα1 X-ray map (panel e) confirms the composition of pure zinc oxide by displaying a very small amount of chlorine. The EM picture (panel a) of SnO_2 in Fig. 7 displays irregularly formed clusters of particles at a 2.5 µm scale. Tin (green) is clearly distributed throughout the sample, according to the EDS layered image (panel b), with some regions displaying overlapping signals.

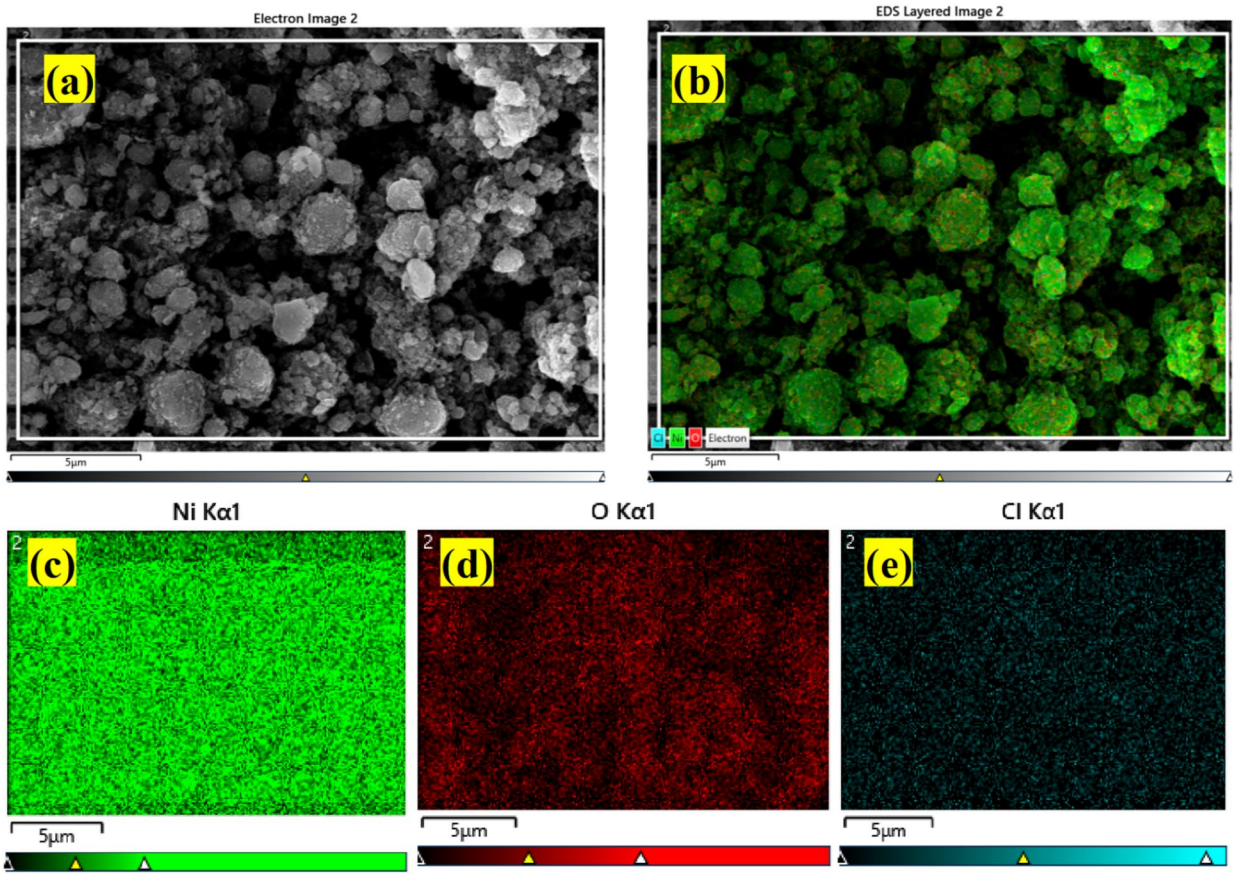

Fig. 5. Distributions of NiO elements and morphology panels (**a**–**e**) include the elements as follows: EM image, EDS layered image, Ni Kα1 X-ray map, O Kα1 map, and Cl Kα1 X-ray map, respectively.

The distribution of tin is shown by the Sn Lα1 X-ray map (panel c), while the existence of oxygen is confirmed by the O Kα1 map (panel d). Moreover, the low chlorine content on the Cl Kα1 map (panel e) indicates no considerable impurities. The composition and distribution of these metal oxides at the micro level are understood by these images, providing complete information on their structural and elemental properties.

Energy dispersive X-ray spectroscopy

The elemental composition and purity of the developed NiO, ZnO, and SnO_2 nanostructured materials are confirmed by the EDS spectra displayed in Fig. 8a–c. The prominent peaks of Zn and O in Fig. 8b demonstrate the synthesis of ZnO, whereas the dominant peaks of Ni and O in Fig. 8a justify the successful formation of NiO. Similarly, the formation of SnO_2 is confirmed by the typical peaks of Sn and O in Fig. 8c, while the weak signals of Cl may come from precursor residues after thorough washing. Their suitability for additional gas-sensing applications is ensured by the overall EDS analysis, which verifies that all three metal oxide nanomaterials were synthesized with great purity and precise proportional composition.

Optical absorption and band gap analysis

Figure 9a–f illustrates the UV–Vis absorption and Tauc plot analysis of the synthesized NiO, ZnO, and SnO_2 nanomaterials. The band gap is determined by Eq. (4).

$$(\alpha h\nu)^n = A(h\nu - E_g) \tag{4}$$

where α is the absorption coefficient, $h\nu$ is the photon energy (eV), A is the proportionality constant, E_g is the optical band gap energy (eV), and n is the electronic transition. In Fig. 9a,b, NiO shows a sharp absorption edge near 390 nm, and the Tauc plot $(\alpha h\nu)^{1/2} = A\ (h\nu\text{-}Eg)$ with $n = 2$ (indirect transition) gives an optical band gap of 2.52 eV. Figure 9c,d presents ZnO with an absorption edge around 400 nm, and from the plot $(\alpha h\nu)^2 = A(h\nu - Eg)$ with $n = 1/2$ (direct transition), a band gap of 2.39 eV is obtained. Similarly, Fig. 9e,f shows SnO_2 exhibiting a clear UV edge, with $n = 1/2$ indicating a direct band gap of 2.32 eV[35]. The observed reduction in band gap values across all samples is attributed to the CTAB surfactant, which alters surface morphology and introduces defect states that enhance charge transfer, thereby improving optoelectronic and gas-sensing performance. The specific optical parameters, such as semiconductor type, absorption edge, and band gap energy, are shown in Table 5.

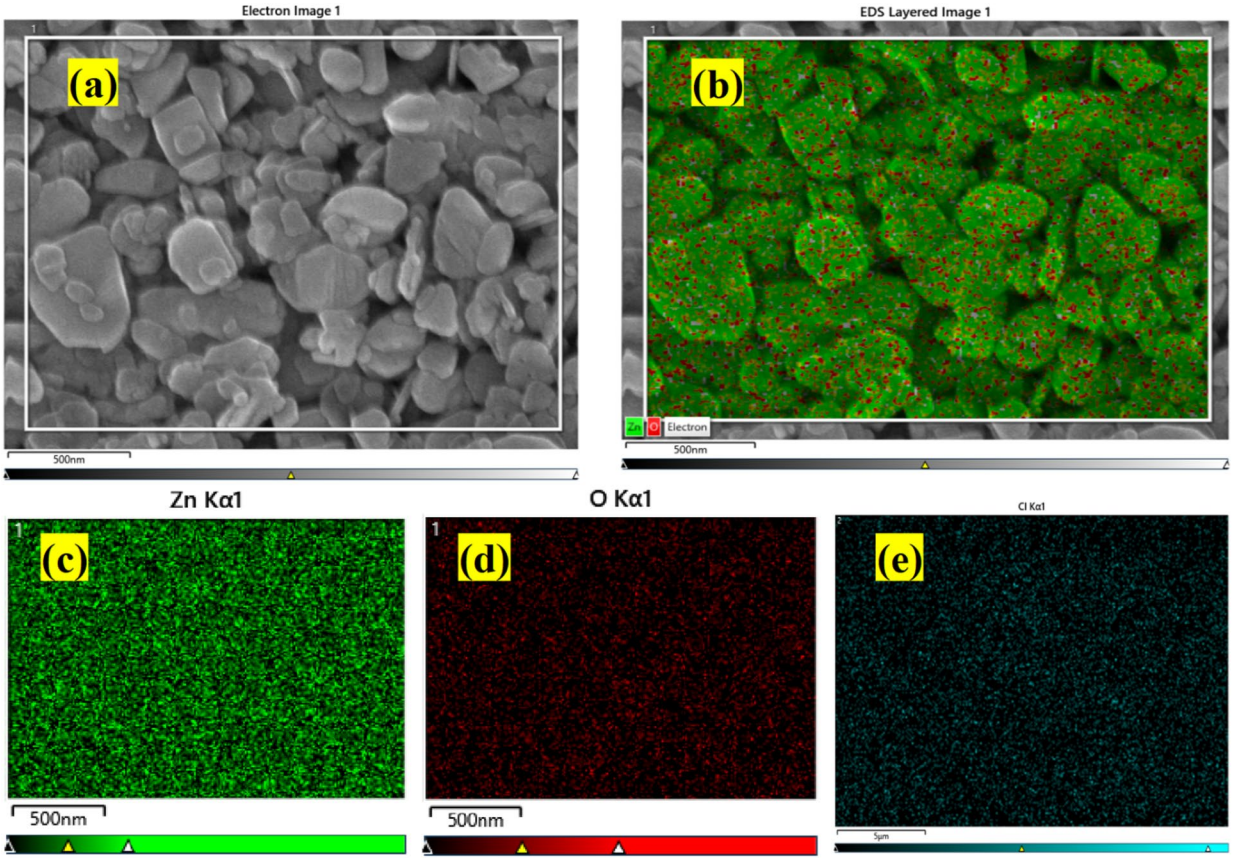

Fig. 6. Elemental and morphological distributions of ZnO panels (**a**,**b**): EM and EDS overlaid images. X-ray maps of Zn Kα1, O Kα1, and Cl Kα1 are shown in panels (**c**–**e**), respectively.

I–V response analysis of surfactant-modified NiO, ZnO, and SnO_2 nanostructures

The I–V characteristics[36] of NiO, ZnO, and SnO_2 nanostructures are presented in Fig. 10. The ohmic contact between the electrodes and the sensing layer is confirmed by the curves' linear and symmetric response to applied voltage. Reliable current conduction and effective charge transfer are guaranteed by this electrical behavior, both of which are necessary for gas sensing to function. The measured current values for NiO, ZnO, and SnO_2 are roughly 0.2×10^{-2} A, 0.4×10^{-2} A, and 1×10^{-2} A, respectively, with an applied bias of 0.2 V. Because of its greater charge carrier mobility and lower interfacial resistance, SnO_2 exhibits a stronger current response, which enhances electron transit across the sensing film. Owing to its p-type conduction and decreased hole mobility, NiO has the least current response, whereas ZnO has a moderate current value. Better gas sensing capability is closely correlated with SnO_2's greater conductivity at 0.2 V. Higher sensitivity and faster response time result from a stronger baseline current, which makes it easier to modulate resistance when target gas molecules are adsorbed. SnO_2 is therefore the most promising of the three materials for resistive-type gas sensing applications since it exhibits the best electrical properties for effective gas adsorption and desorption reactions.

EIS characterization of surfactant-assisted SnO_2, ZnO, and NiO nanostructures

As shown in Fig. 11, the electrochemical impedance spectroscopy (EIS) investigation[37] identifies unique electrical properties for NiO, ZnO, and SnO_2 sensing materials.

NiO shows the highest charge transfer resistance (R_{ct}) of about 2.1 kΩ among the samples, suggesting a comparatively slower electron transit and limited conductivity. This could be because NiO is a p-type semiconducting material with fewer accessible charge carriers. In contrast, ZnO exhibits a moderate resistance of 0.8 kΩ, which is indicative of higher electrical conductivity because of its enhanced carrier mobility and n-type properties. At 0.45 kΩ, SnO_2 exhibits the lowest resistance, indicating the most effective charge transfer capacity and improved interfacial contact between the surface and the adsorbed gas molecules. Table 6 shows that on reducing the resistance from NiO to SnO_2, capacitance increases and relaxation frequency (f_{max}) changes, which indicate quicker response and recovery characteristics. The findings demonstrate that compared to NiO and ZnO, SnO_2 has superior electrochemical performance, making it more suitable for rapid and sensitive gas sensing.

The relationship between BET surface area analysis and gas sensing behavior

The nitrogen adsorption–desorption isotherms of NiO, ZnO, and SnO_2 nanostructures are displayed in Fig. 12a. The presence of mesoporous structures that promote gas diffusion and adsorption is confirmed by the

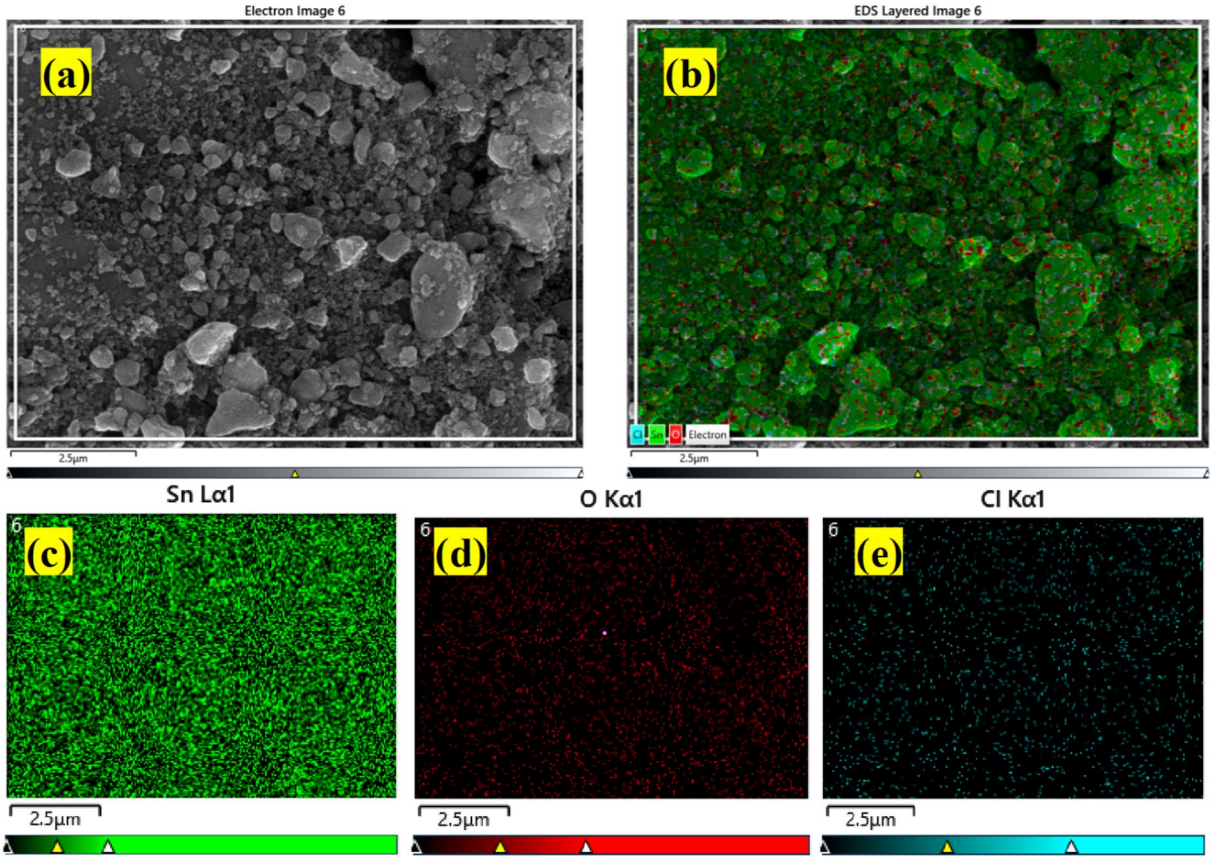

Fig. 7. Distributions of SnO_2 in morphology and elements EM image (**a**), EDS layered image (**b**), X-ray maps of Sn Kα1, O Kα1, and Cl Kα1 (**c**).

characteristic type IV isotherm with a H_2-type hysteresis loop demonstrated by all samples. Monolayer adsorption is responsible for the slow increase in adsorption at lower relative pressures ($P/P_o < 0.3$), but multilayer adsorption and capillary condensation within mesopores are responsible for the sharp increase at higher pressures ($P/P_o > 0.8$). SnO_2 has the largest absorption of nitrogen of all the materials under study, followed by ZnO and NiO, indicating a bigger surface area and higher pore volume. Because it increases the availability of active sites and speeds up gas–solid interactions, the presence of such mesoporous frameworks is crucial for gas sensors[38,39]. The linearized BET plots for NiO, ZnO, and SnO_2 are shown in Fig. 12b. As shown in Table 7, surface area, pore volume, and pore diameter were computed using the acquired slope and intercept values. Accuracy of the BET data is confirmed by the plots' linearity ($R^2 = 0.998$). With the biggest surface area and most consistent pore distribution, SnO_2 shows the lowest slope and highest R^2 value. These textural properties contribute to improved surface reaction rates and quick gas diffusion, which directly affect the sensor response and recovery times.

Correlation between BET data and gas sensing mechanism The BET surface study can infer that surface morphology and porosity exert a great influence on gas sensing efficiency. SnO_2 possesses the largest specific surface area and smallest pore width and shows a well-developed mesoporous structure, facilitating efficient gas adsorption. In this work, SnO_2 exhibits such an ideal characteristic, which brings about an improvement in selectivity, fast recovery, and enhanced sensing response. ZnO, a p-type semiconductor, has a moderate surface area and pore width and thus exhibits adequate gas diffusion behavior, while NiO, a semiconductor with inferior surface areas, provides fewer active adsorption sites and hence lower gas sensitivity. Moreover, the mesoporous structure of SnO_2 assured reliable and repeatable adsorption cycles, in good agreement with Gibson et al.'s[40] work, where an important relation between BET surface properties and stability of the gas response has been identified. SnO_2 is much better in gas sensing compared to the other two oxides under investigation due to its higher specific surface area, improved pore structure, and more efficient charge exchange mechanism between adsorbed gas molecules and surface oxygen species. The PEDOT: PSS/Oxide heterojunction is considered to be responsible for the increased current and reduced interfacial resistance as it offers an efficient charge transfer route.

Gas sensing experimental setup and working principle

Figure 13 presents the experimental setup[41] schematically to assess the gas sensing performance of fabricated sensors based on NiO, ZnO, and SnO_2 towards CO and CH_4 gases. The system consists of a stainless steel gas chamber with a controlled heater and is also equipped with mass flow controls (MFCs) and accurate gas supply lines connected with traditional gas cylinders containing CO, CH_4, and N_2. Nitrogen is used as the carrier and

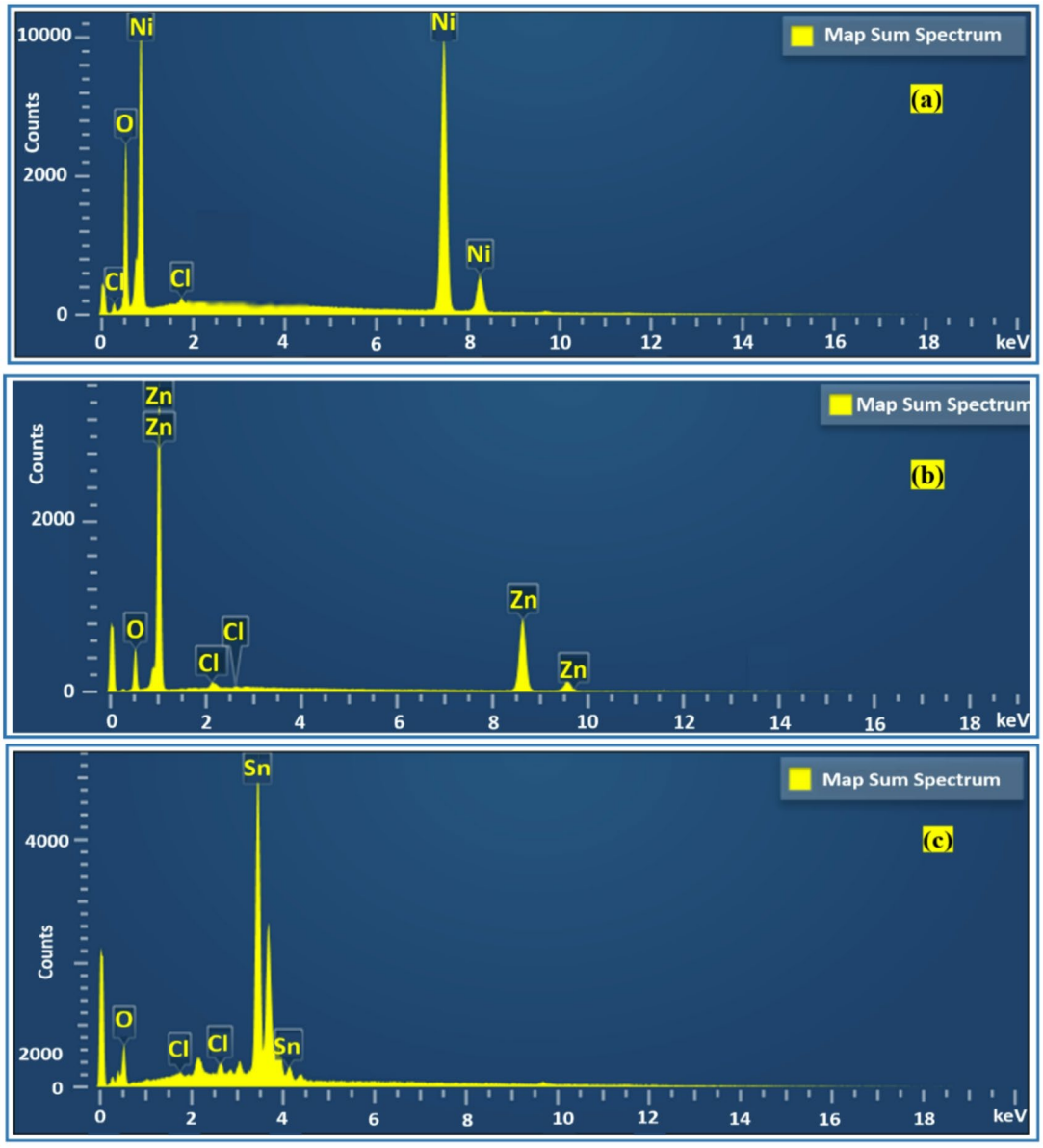

Fig. 8. EDS spectra of (**a**) NiO, (**b**) ZnO, and (**c**) SnO_2 nano materials.

purging gas in order to dilute the other gases accurately and remove any leftover gas in between successive measurements. The sensor element is fixed on a heating platform inside the gas chamber, which keeps the working temperature steady and tailored to the needs of each material. The heater is connected to a programmable DC power supply to precisely regulate the working temperature, as gas sensing responses in metal oxides are strongly temperature-dependent. Electrical connections from the sensor are routed to a Keithley source meter, which records real-time resistance or current changes during gas exposure. The mass flow controllers precisely regulate the flow rate and concentration of the test gases. The target gas (CO and CH_4) is mixed with carrier nitrogen to achieve the desired ppm-level concentration before entering the chamber. Once the gas mixture reaches equilibrium within the chamber, the variation in sensor resistance is recorded continuously. Upon completion of the gas exposure cycle, pure N_2 is passed again to remove residual gas molecules and to allow the sensor to recover to its baseline resistance value.

Gas sensing mechanism

Gas sensing mechanism for CTAB-Assisted NiO, ZnO, and SnO_2 Nanostructures Toward CO and CH_4 is shown in Fig. 14. The mechanism of gas sensing for CTAB-assisted NiO[42], ZnO, and SnO_2 nanostructures toward CO and CH_4 (Fig. 14a,b) is mainly dominated by the adsorption of atmospheric oxygen along with a redox interaction between chemisorbed oxygen ions and the reducing gases. Upon exposing the sensor to air, oxygen molecules adsorb on the metal oxide surface, extracting electrons from either the conduction band (n-type) or the valence band (p-type), to yield ionic surface oxygen species. It can be represented as Eqs. (5–7)[43].

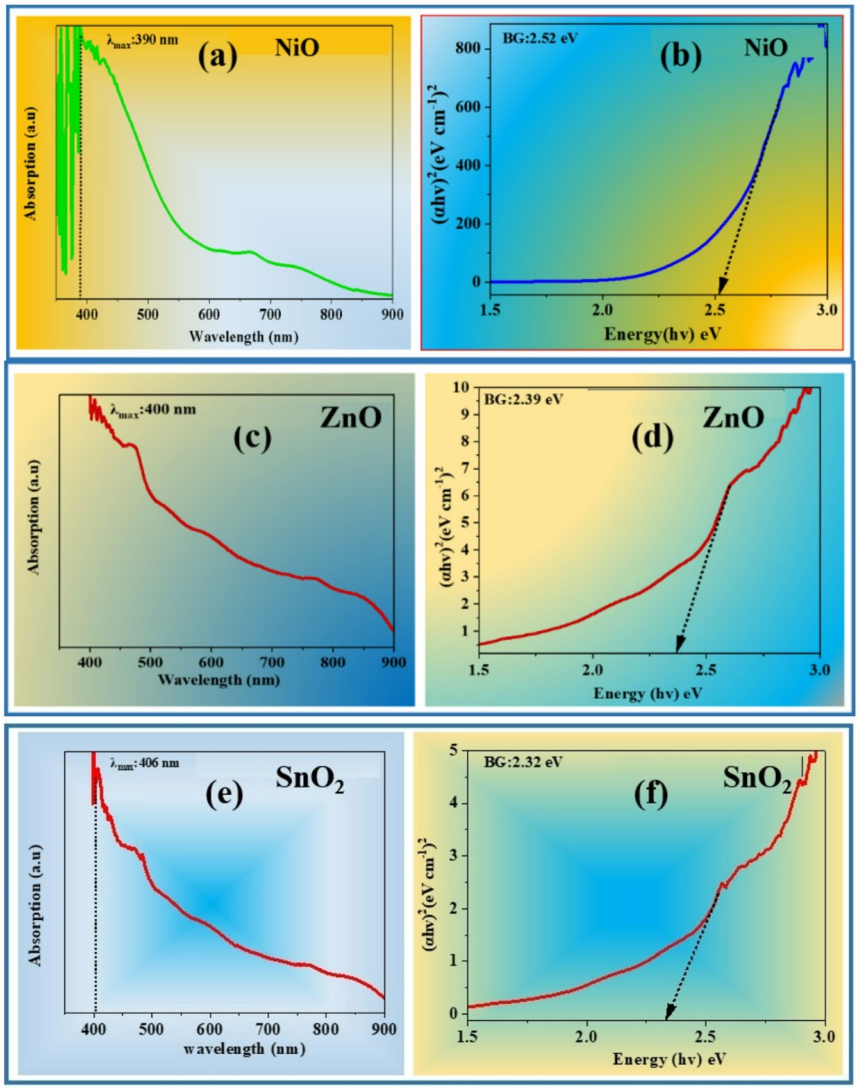

Fig. 9. (**a**,**c**,**e**) Optical absorption of NiO, ZnO, SnO_2, and (**b**,**d**,**f**) Band gap analysis of sized NiO, ZnO, SnO_2 nanomaterials, respectively.

Material	Type of semiconductor	Absorption edge (λ_{max})	Band gap (eV)	Inference
NiO	p-type	~390 nm	2.52	Limited hole mobility and slower surface reactivity
ZnO	n-type	~400 nm	2.39	Faster electron transport and strong oxygen adsorption
SnO_2	n-type	~380 nm	2.32	Highest surface activity, enhanced charge transfer efficiency

Table 5. Comparative analysis of NiO, ZnO, and SnO_2 nanomaterials for gas sensing performance.

$$O_2\,(gas) \rightarrow O_2{}^-\,(ads) \tag{5}$$

$$O_2\,(gas) + e^- \rightarrow O^-\,(ads) \tag{6}$$

$$O\,(gas) + 2e^- \rightarrow O^{2-}\,(ads) \tag{7}$$

These reactions result in a surface depletion layer due to electron withdrawal, thereby increasing the resistance of n-type ZnO and SnO_2.

The PEDOT: PSS overlayer forms a p–n heterojunction[44] with the n-type metal oxide (ZnO and SnO_2), creating a built-in electric field which enhances the electron exchange during gas adsorption and, accordingly, accelerates resistance modulation. Such an interfacial effect brings about sensitivity enhancement and faster response–recovery behavior. In contrast, electron removal in p-type NiO increases the hole concentration, thus

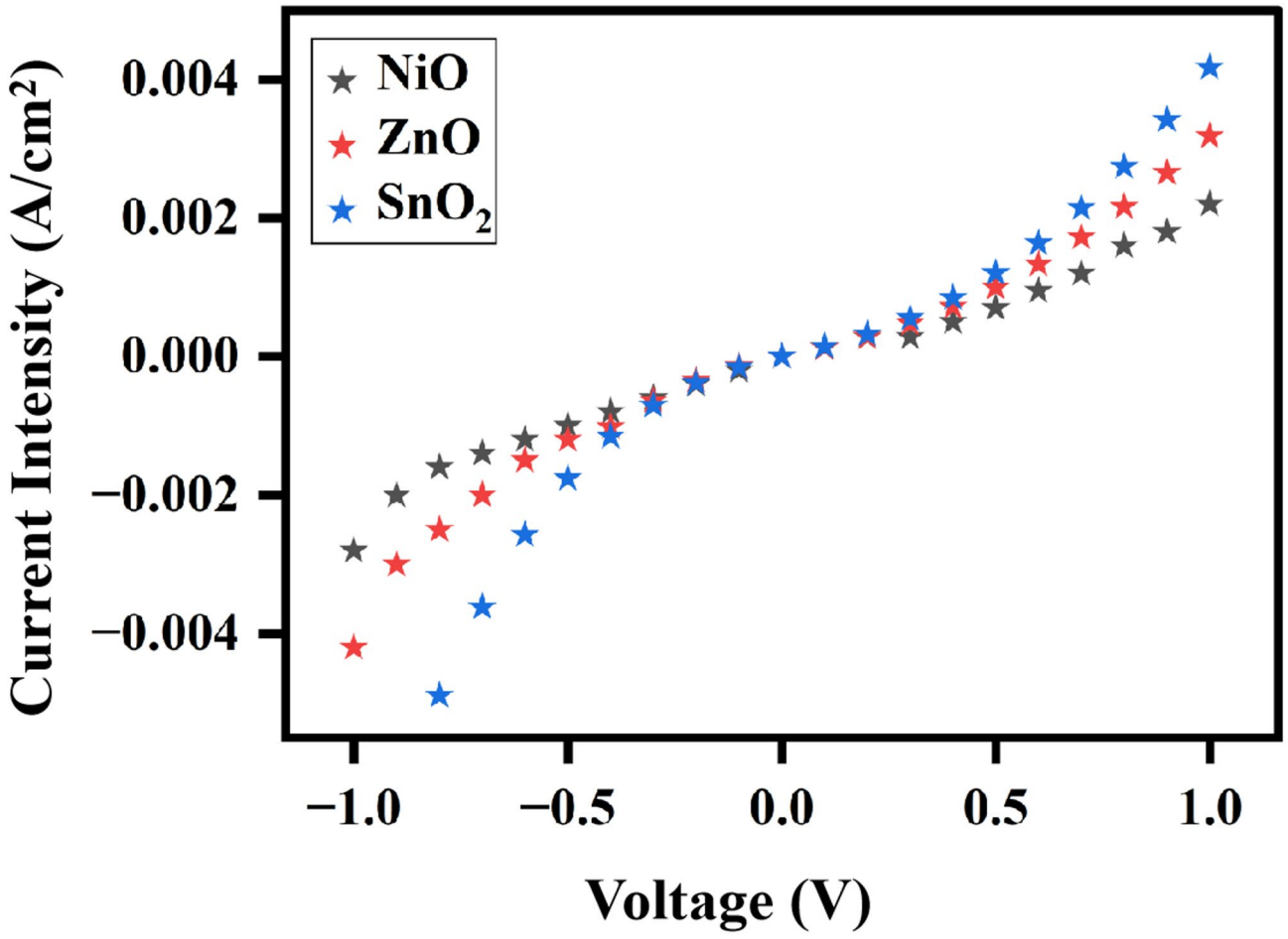

Fig. 10. I–V properties of ZnO, NiO, and SnO_2 nanostructures measured between − 1.0 and + 1.0 V.

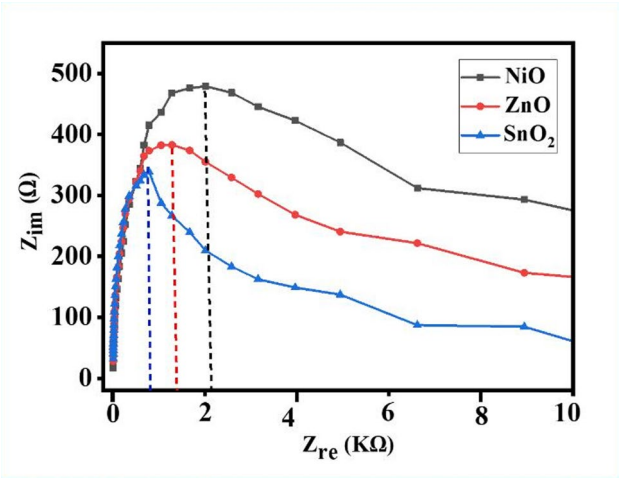

Fig. 11. Nyquist plots of NiO, ZnO, and SnO_2 at room temperature (Z_{re} vs. Z_{im}).

Sample	R_{ct} (Ω)	C_{dl} (μF)	f_{max} (Hz)
NiO	2100	147.48 μF	0.514 Hz
ZnO	800	233.12 μF	0.853 Hz
SnO_2	450	294.08 μF	1.203 Hz

Table 6. EIS parameters showing capacitance values (C_{dl}), f_{max}, and R_{ct} for NiO, ZnO, and SnO_2.

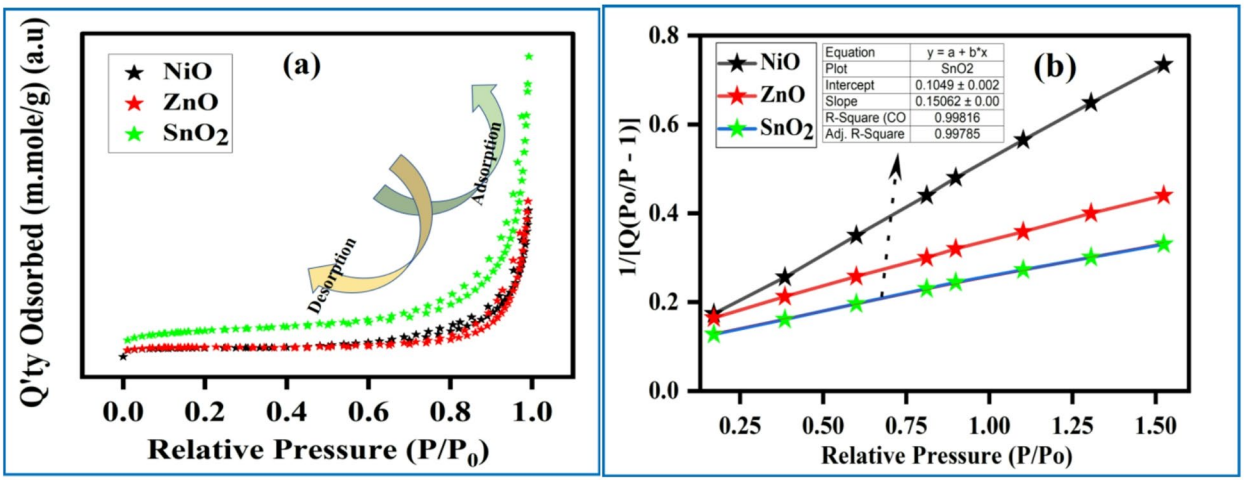

Fig. 12. (**a**) Adsorption–desorption isotherms for N_2, (**b**) The BET surface area of SnO_2, ZnO, and NiO samples.

Material	Slope	Intercept	R^2	Surface area (m^2/g)	Pore volume (cm^3/g)	Pore diameter (nm)
NiO	0.1506	0.1049	0.9981	27.43	0.082	9.4
ZnO	0.1184	0.1067	0.9980	41.25	0.096	8.7
SnO_2	0.1050	0.1049	0.9978	59.62	0.115	7.8

Table 7. BET surface area and pore characteristics of NiO, ZnO, and SnO_2 nanostructures.

forming an accumulation layer and decreasing the baseline resistance. When exposed to reducing gases such as CO and CH_4, the gas molecules react with these ionized oxygen species. This reaction injects electrons back into the semiconductor, directly modulating the resistance. The reactions proceed according to Eqs. (8) and (9).

$$CO + O^- \rightarrow CO_2 + e^- \tag{8}$$

$$CH_4 + 4O^- \rightarrow CO_2 + 2H_2O + 4e^- \tag{9}$$

The electrons that return to n-type ZnO/SnO_2 decrease the width of the depletion layer and sharply reduce the resistance.

In p-type NiO, electrons neutralize holes and reduce the hole concentration, hence increasing the resistance. Accordingly, surface area enhancement, prevention of particle agglomeration, and the addition of more active adsorption sites are some of the important roles played by CTAB. This accelerates the reaction between surface oxygen ions and target gases due to enhanced gas diffusion. Among the materials proposed, SnO_2 shows the strongest response due to its higher oxygen-vacancy density, providing more electron-trapping sites and thereby allowing for stronger charge-transfer interactions.

Room-temperature gas sensing pathway

Because of the unavailable activation energies to form O^- or O^{2-} at room temperature, superoxide O_2^-(ads) is the dominant adsorbed oxygen species. The mechanism of adsorption can be expressed as given in Eq. (10).

$$O_2\,(g) + e^- \rightarrow O_2^-\,(ads) \tag{10}$$

Thus, at ambient conditions, all the subsequent redox reactions are determined by O_2^-(ads). In the presence of reducing gases[45]:

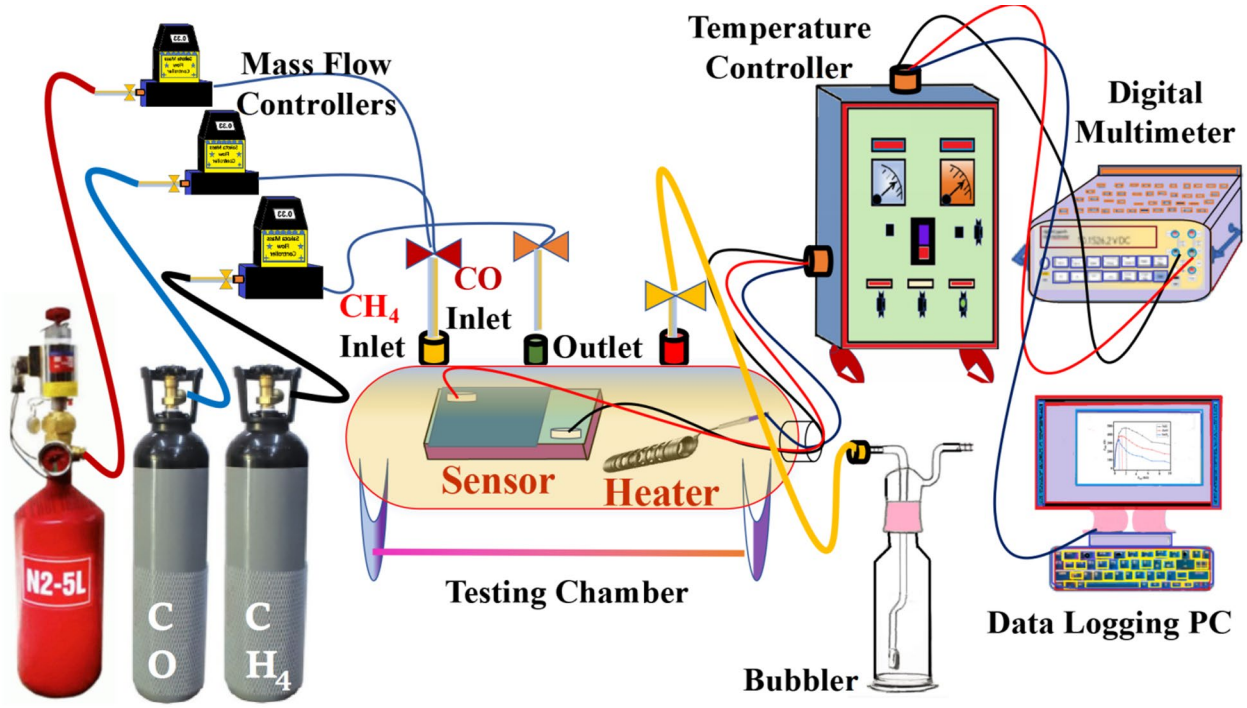

Fig. 13. A schematic diagram of experimental gas sensing setup.

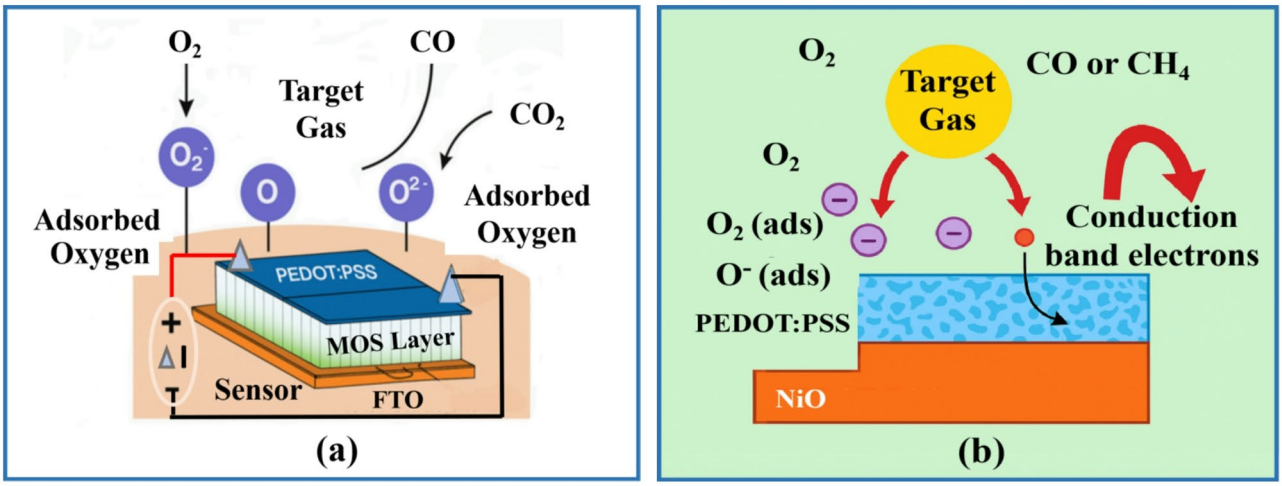

Fig. 14. Gas sensing mechanism for CTAB-assisted NiO, ZnO, and SnO_2 nanostructures toward CO and CH_4 (**a**) at room-temperature gas sensing, and (**b**) PEDOT: PSS/NiO (p–p heterojunction).

$$CO\,(g) + O_2{}^-\,(ads) \rightarrow CO_2\,(g) + e^- \tag{11}$$

$$CH_4\,(g) + 4O_2{}^-\,(ads) \rightarrow CO_2\,(g) + 2H_2O\,(g) + 4e^- \tag{12}$$

Both reactions free electrons, reducing the depletion region of ZnO/SnO_2 and producing measurable changes in resistance. Under 52–55% relative humidity (RH), the water molecules partially dissociate on the oxide surface as shown in Eq. (13)[46].

$$H_2O\,(ads) - OH\,(surface) + H^+ \tag{13}$$

These hydroxyl groups are in slight competition with oxygen adsorption, but their influence is minimized due to the stabilizing effect of the PEDOT: PSS overlayer. The PEDOT: PSS/oxide interface provides an additional path for charge transport, thus granting stable and humidity-tolerant sensing behavior.

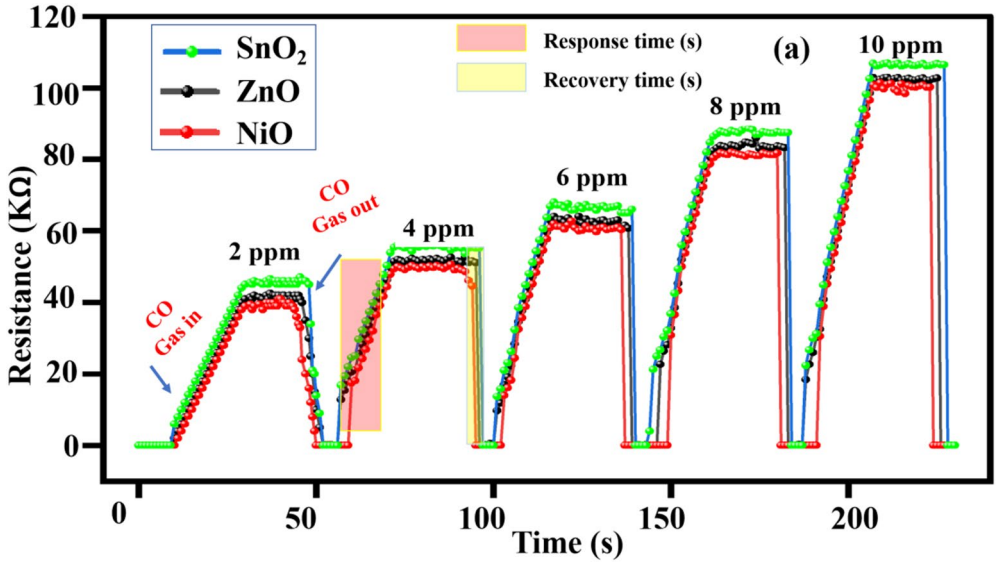

Fig. 15. Gas sensors based on NiO, ZnO, and SnO_2 nanostructures exhibit dynamic response and recovery behavior when exposed to (**a**) CO and, (**b**) CH_4 gases at ambient temperature.

Mechanism of PEDOT: PSS/NiO p–p heterojunction

In the case of NiO[47,48], combined with PEDOT: PSS, its sensing mechanism is dominated by hole modulation across a p-p heterojunction. Thus, oxygen adsorption increases hole concentration in both layers, reducing resistance. The oxygen species are formed as given in Eqs. (14) and (15).

$$O_2\,(g)\ + 2H^+ \rightarrow 2O^-\,(ads) \tag{14}$$

$$O_2\,(g)\ + H^+ \rightarrow {O_2}^-\,(ads) \tag{15}$$

$$CH_4 + 4O^- \rightarrow CO_2 + 2H_2O + 4e^- \tag{16}$$

In the presence of reducing gases, electrons are released according to Eq. (16), which recombine with holes ($e^- + H^+ \rightarrow$ null), decreasing the hole concentration in PEDOT: PSS and NiO. Therefore, the resistance increases. The p–p interface enables fast transport[49] of holes that enhances interfacial charge transfer and thus leads to enhanced sensitivity and selectivity toward CO and CH_4.

Performance characteristics

Response/recovery time study

Figure 15a presents the dynamic response of SnO_2, ZnO, and NiO sensors towards various CO gas concentrations in a range of 2–10 ppm. Each sensing cycle consists of a fast increase in resistance, so-called "Gas in," when the sensor is exposed to CO, and subsequent decay to baseline, so-called "Gas out," when CO is removed. All three sensors demonstrate excellent reliability and reversibility of the response-recovery characteristics, which are identical and reproducible. The biggest magnitude of response through all concentrations of the SnO_2-based sensor proves its superior surface reactivity toward CO molecules. The sensor based on ZnO shows moderate response intensity, while that of NiO has the lowest amplitude of response due to slower charge transfer and fewer adsorption sites. The presence of oxygen vacancies and efficient electron exchange between CO molecules and adsorbed oxygen species accounts for such a fast reaction and recovery of SnO_2, indicating enhanced electron transport at the surface and faster adsorption–desorption kinetics. Compared to ZnO and NiO, this enhanced performance implies that SnO_2 provides a more effective surface reaction dynamics approach. When exposed to CH_4 gas at ambient temperature, the dynamic response and recovery behavior of gas sensors based on NiO, ZnO, and SnO_2 nanostructures are shown in Fig. 15b[50]. The gas adsorption and desorption cycles are represented by each rise and fall in the curve, respectively. All samples' resistance quickly rises when exposed to CH_4 because the sensor surface's adsorbed oxygen ions are reduced, which lowers the availability of electrons in the conduction band. The initial resistance level is restored when the gas supply is cut off because oxygen molecules are adsorbed on the surface. SnO_2 shows the largest resistance modulation among the materials studied, suggesting improved adsorption capacity and higher surface contact with CH_4 molecules. NiO has comparatively less resistance fluctuation than ZnO, which exhibits moderate response behavior. Fast electron interaction between the gas species and the sensor surface is reflected in the resistance's sharp peak and decrease. In comparison to ZnO (18 s/10 s) and NiO (20 s/12 s), the SnO_2-based sensor exhibits a response time of 15 s and a recovery time of 8 s. The outstanding repeatability and stability of the sensing films are confirmed by the steady cycle response.

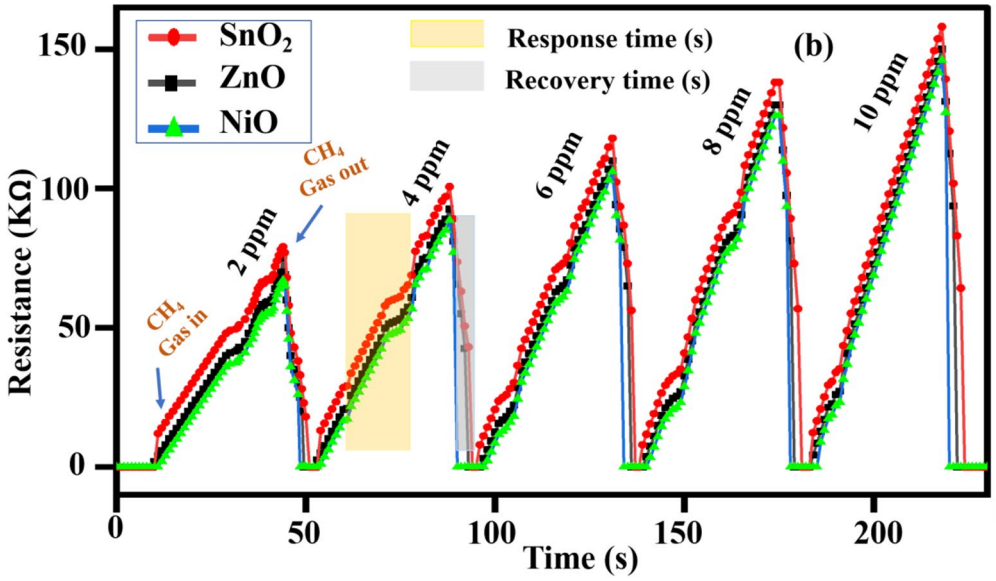

Fig. 15. (continued)

Sensitivity

As shown in Fig. 16, the sensitivity of the manufactured metal oxide sensors was assessed for CO gas concentrations between 2 and 10 ppm. Equation (17)[51] defines sensitivity as the relative change in resistance following exposure to gas.

$$S = \frac{R_g - R_a}{R_a} \times 100 \tag{17}$$

Here, R_g is the resistance of the sensor in the target gas (ppm); the baseline resistance, R_a, measured in air, was about 1200 KΩ for ZnO, 1800 KΩ for NiO, and 450 KΩ for SnO_2 at room temperature. The baseline drift during repeated sensing cycles did not exceed ± 2–3% for ZnO, ± 3–4% for NiO, and ± 1–2% for SnO_2, demonstrating good resistance stability under ambient conditions. Out of the three materials under investigation, the SnO_2-based sensor had the highest sensitivity and a noticeable rise in resistance as the CO concentration increased. This improvement is ascribed to SnO_2's greater quantity of surface-active sites and plentiful oxygen vacancies, which facilitate effective CO molecule adsorption and quicken surface electron exchange reactions. As seen in Table 8, NiO exhibited the least response because of its restricted carrier modulation during gas adsorption and

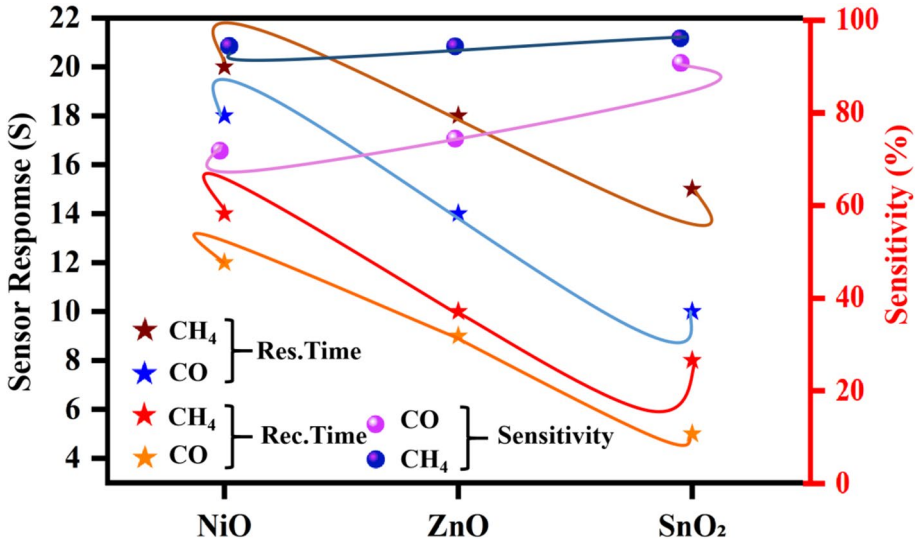

Fig. 16. Sensor response characteristics showing the sensitivity and response time for various gases (CO, CH_4) using different metal oxide materials (NiO, ZnO and SnO_2).

Material	CO gas		CH_4 gas		Sensitivity (%)	
	Response time (S)	Recovery time (S)	Response time (S)	Recovery time (S)	CO gas	CH_4 gas
NiO	18	12	20	12	64.7	87.5
ZnO	14	9	18	10	78.6	89.6
SnO_2	10	5	15	8	92.3	90.8

Table 8. Response and recovery time of NiO, ZnO, and SnO_2 nanostructures toward CO and CH_4 Gases.

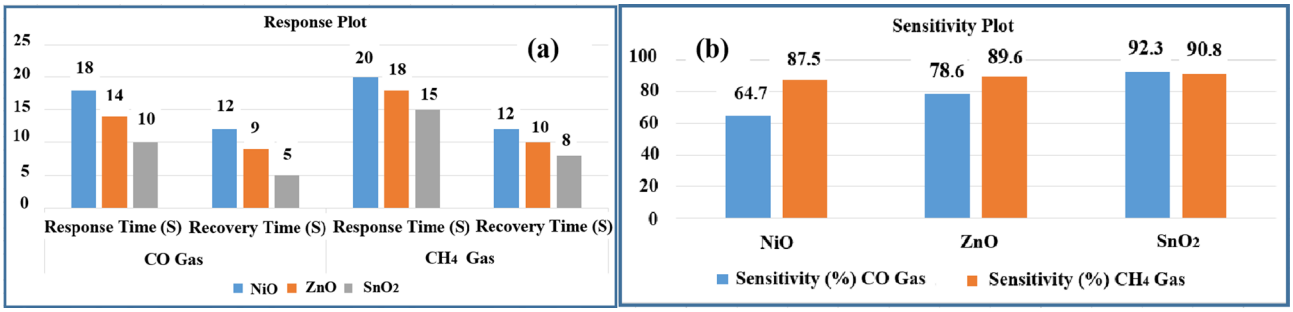

Fig. 17. Gas sensing performance of NiO, ZnO, and SnO_2 sensors. (**a**) Response and recovery times for CO and NO gases. (**b**) Sensitivity (%) for NO and CO gases.

reduced surface reactivity, whereas ZnO displayed intermediate sensitivity. The SnO_2 sensor had a sensitivity of about 92.3% at 10 ppm CO, while ZnO and NiO had a sensitivity of 78.6% and 64.7%, respectively. Due in large part to its high surface-to-volume ratio, robust interaction with reducing gases, and improved charge transfer kinetics at the sensing interface, these results validate that the SnO_2 nanostructure provides superior gas-sensing behavior. Figure 17 presents a comparative analysis of the gas sensing properties of ZnO and SnO_2. The figure includes a response plot measuring the response and recovery times for CO and CH_4 gases, and a sensitivity plot showing the corresponding sensitivity percentages for each gas.

Influence of humidity on sensor performance The presence of water molecules that compete with the target gases for adsorption sites is known to influence the surface reaction of MOS-based gas sensors. For this reason, all gas sensing experiments in this work were conducted under controlled ambient humidity conditions from 52 to 55% RH. Within this range, only a very negligible variation in response amplitude and baseline resistance was observed. Overall, the net change in response due to humidity is within ± 3%, ± 4%, and ± 2% for ZnO, NiO, and SnO_2, respectively, which indicates the stable operation of the sensors at typical room conditions. The SnO_2 device exhibited the highest tolerance against humidity because it possesses a relatively compact surface morphology and presumably displays lower affinity for water adsorption, compared to NiO and ZnO. Finally, this PEDOT: PSS/metal oxide heterojunction stabilizes the surface charge transfer process, which suppresses further humidity interference. These results confirm that the proposed sensors can reliably detect CO and CH_4 without significant influences emanating from ambient humidity fluctuations.

Gas sensing performance comparison
Based on the performance metrics summarized in Table 9, the SnO_2+CTAB sensor developed in this work demonstrates superior carbon monoxide detection capabilities, operating efficiently at room temperature with a sensitivity of 92.3% for 10 ppm CO. This represents a significant enhancement over previously reported SnO_2 nanoparticles, which required an operating temperature of 300 °C to achieve 87% sensitivity. Furthermore, compared to a number of reference materials that operate at high temperatures, including ZnO nanorods at 700 °C, the sensor shows quick reaction and recovery durations of 10 s and 5 s, respectively. Room-temperature functioning, rapid kinetics, and high sensitivity make the SnO_2+CTAB composite a very attractive material for low-power, high-performance real-world applications.

Long-term stability analysis
Long-term operational stability[55] is an indispensable prerequisite for the practical application of gas sensors. For this evaluation, the baseline resistance of the fabricated sensors was continuously monitored over a period of 30 days upon repeated exposure to CO and CH_4 in the concentration range of 2–20 ppm. Figure 18a (CO sensing) and Fig. 18b (CH_4 sensing) illustrate the temporal variations in resistance for all concentrations under test. During the 30-day test period, both sensing environments exhibited only a slight drift. Although the resistance at lower concentrations (2 ppm) deviated little, it remained within a reasonable range; thus, variations at higher concentrations in the range of 5–20 ppm remained consistently small and stable. This suggests that the devices retain excellent repeatability and structural integrity over an extended usage period. The PEDOT: PSS/ SnO_2 heterojunction sensor showed the most stable behavior due to its compact surface morphology and stabilized

Material	Target gas	Concentration (ppm)	Operating temp. (°C)	Sensitivity/response (%)	Response time (s)	Recovery time (s)	Ref.
ZnO Nanorods	CO	100	700	88	60	40	[52]
SnO_2 Nanoparticles	CO	10	300	87	85	65	[53]
ZnO/SnO_2 Nanosheets	VOC	1	200	64	10	50	[54]
NiO Nanoflowers	H_2	500	300	45	54	15	[7]
SnO_2 + CTAB	CO	10	Room Temp.	92.3	10	5	This work

Table 9. Comparison of the proposed SnO_2 sensor's gas detection performance with that of existing sensors.

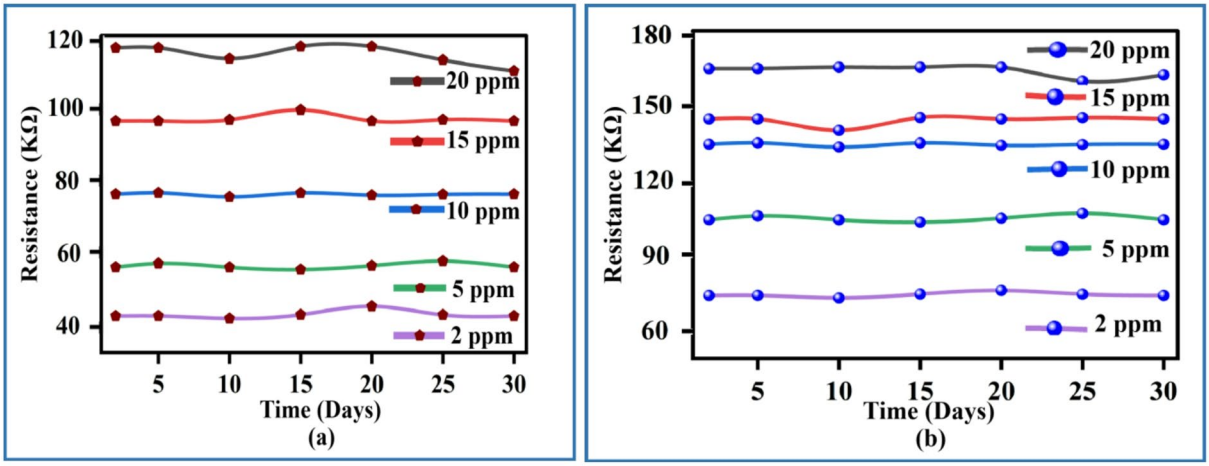

Fig. 18. Long-term stability of the fabricated gas sensors over 30 days: (**a**) Resistance variation of the sensor toward CO at different concentrations (2, 5, 10, 15, and 20 ppm). (**b**) Resistance variation of the sensor toward CH_4 at the same concentration range.

interfacial charge-transfer characteristics. Overall, these results assure good long-term stability for the proposed sensors to ensure reliable and reproducible detection of CO and CH_4 gases under realistic operating conditions.

Conclusion

The comprehensive findings of this investigation indicate that the successful production of extremely effective room-temperature gas sensors was made possible by the strategic fusion of heterojunction engineering and CTAB-mediated synthesis. PEDOT: PSS incorporation and consequently the formed p–n heterojunction played a crucial role in enhancing sensitivity and allowed for fast room-temperature detection. The ideal parameters of the SnO_2 nanostructures were determined by material characterisation. These included a low internal resistance of 0.45 kΩ, a large surface area of 59.62 m^2/g, an adequate band gap of 2.32 eV, and a minimal crystallite size of 2.32 nm. As shown in Table 1, the fabricated PEDOT: PSS/SnO_2 heterojunction sensor performed exceptionally well, showing higher sensitivity to both CO (92.3%) and CH_4 (90.8%) than the NiO and ZnO-based sensors. Additionally, with the quickest response and recovery times of 10/5 seconds for CO and 15/8 seconds for CH_4, the SnO_2-based device demonstrated the fastest reaction dynamics. Throughout several testing cycles, the sensor also demonstrated outstanding repeatability and a linear response. These results obviously demonstrate the improvement in sensing capabilities due to a combination of the effects related to the increased surface area, improved charge transport, and nanostructure of the p-n heterojunction. The present work thereby confirms that the method proposed here is a viable and promising approach toward the development of next-generation compact gas sensors for environmental and human health applications.

Data availability

The datasets used and/or analysed during the current study available from the corresponding author on reasonable request.

Received: 26 October 2025; Accepted: 24 December 2025
Published online: 31 December 2025

References

1. Liu, X., Ma, T., Pinna, N. & Zhang, J. Two-dimensional nanostructured materials for gas sensing. *Adv. Funct. Mater.* **27** (37), 1702168 (2017).
2. Wang, C., Yin, L., Zhang, L., Xiang, D. & Gao, R. Metal oxide gas sensors: sensitivity and influencing factors. *Sensors* **10** (3), 2088–2106 (2010).

3. Kumar, R., Liu, X., Zhang, J. & Kumar, M. Room-temperature gas sensors under photoactivation: from metal oxides to 2D materials. *Nano-micro Lett.* **12** (1), 164 (2020).
4. Chowdhury, A. P., Anantharaju, K. S. & Keshavamurthy, K. Inorganic nanomaterials for senor applications. In *Multifunctional Inorganic Nanomaterials*, 147–157 (CRC, 2025).
5. Güell, F. et al. ZnO-based nanomaterials approach for photocatalytic and sensing applications: recent progress and trends. *Mater. Adv.* **4** (17), 3685–3707 (2023).
6. Wang, D. et al. Pd-Modified SnO_2 octahedrons for Humidity-Independent ethanol vapor gas sensing. *J. Alloys Compd.* 180635 (2025).
7. Kaur, N. Nickel oxide nanostructures for gas sensing: recent Advances, Challenges, and future perspectives. *ACS Sens.* **10** (3), 1641–1674 (2025).
8. Suryawanshi, M. H. K. & Yenorkar, S. M. A review of semiconductor metal oxides for hydrogen sulfide and methane gas detection. *IJSAT-Int. J. Sci. Technol.* **16**(1). (2025).
9. Wang, C. N. et al. Advances in doped ZnO nanostructures for gas sensor. *Chem. Record*. **20** (12), 1553–1567 (2020).
10. Liu, M. et al. Effect of CTAB on the morphology of Sn-MOF and the gas sensing performance of SnO_2 with different crystal phases for H_2 detection. *Chemosensors* **13** (5), 192 (2025).
11. Wang, Y., Zhang, L., Liu, X., Wang, Z. & Zhang, T. High-performance room-temperature NO_2 sensor based on PEDOT:PSS/SnO_2 heterojunction nanofibers. *Chem. Eng. J.* **471**, 144568 (2023).
12. Yan, Y. et al. Conducting polymer-inorganic nanocomposite-based gas sensors: a review. *Sci. Technol. Adv. Mater.* **21** (1), 768–786 (2020).
13. Uma, B. et al. Fabrication of Zirconia-doped Cu_2O/CuO/Cu hetero-nanocomposite: Enhanced electrochemical sensor, antibacterial and photocatalytic activity. *Ionics*. 1–18 (2025).
14. Shi, W., Song, S. & Zhang, H. Hydrothermal synthetic strategies of inorganic semiconducting nanostructures. *Chem. Soc. Rev.* **42** (13), 5714–5743 (2013).
15. Abbas, S. R. & Oleiwi, H. F. ZnO Nanorod arrays for gas sensor application growing via hydrothermal technique: effect of metal oxide decoration. *J. Opt.* 1–11 (2024).
16. Sharma, K. K. et al. Synthesis of nanostructured cubic phase SnO_2 thin film and its trace-level sensing of CO gas. *Nat. Commun.* (2025).
17. Jaiswal, A., Kang, S. G., Kumar, R. & Hur, S. H. Tailoring defect generation in SnO_2 nanostructure for increased selectivity in electrochemical CO_2 reduction. *Nanoscale* (2025).
18. Taher, F. A. & Abdeltwab, E. Chemical approaches for 1D oxide nanostructures. In *Nanomaterials Synthesis*, 53–83 (Elsevier, 2019).
19. Beduk, T. et al. A paper-based inkjet-printed PEDOT: PSS/ZnO sol-gel hydrazine sensor. *Sens. Actuators B*. **306**, 127539 (2020).
20. Dutta, P. & Gupta, G. Environmental gas sensors based on electroactive hybrid organic–inorganic nanocomposites using nanostructured materials. *Phys. Chem. Chem. Phys.* **24** (47), 28680–28699 (2022).
21. Zhang, Y., Feng, W. & Ullah, A. Room-temperature highly sensitive CO gas sensor based on Au-modified SnO_2/ZnO. *J. Mater. Sci. Mater. Electron.* **36** (25), 1–13 (2025).
22. Chowdhury, A. P., Anantharaju, K. S., Keshavamurthy, K., Swain, S. & Uma, B. A mini-review on Z and S scheme heterojunction bismuth based photocatalysts towards H_2 production, CO_2 reduction, and pollutant degradation. *Next Mater.* **8**, 100918 (2025).
23. Akhtar, M., Shahzadi, S., Arshad, M., Akhtar, T. & Janjua, M. R. S. A. Metal oxide-polymer hybrid composites: a comprehensive review on synthesis and multifunctional applications. *RSC Adv.* **15** (23), 18173–18208 (2025).
24. Goswami, Y. C., Bisauriya, R., Goswami, R., Hlaing, A. A. & Moe, T. T. Hydrothermal synthesis of SnO_2/cellulose nanocomposites: optical, Structural, and morphological characterization. *Sci. Rep.* **15** (1), 9752 (2025).
25. Boudour, S. et al. Crystalline structure, morphology, and topography analysis of spin-coated ZnO and zno: S microstructures. *Phys. B: Condens. Matter* 417708 (2025).
26. Singh, A. et al. Structurally and morphologically engineered single-pot biogenic synthesis of NiO nanoparticles with enhanced photocatalytic and antimicrobial activities. *J. Clean. Prod.* **343**, 131026 (2022).
27. Jayswal, S. & Moirangthem, R. S. Thermal decomposition route to synthesize ZnO nanoparticles for photocatalytic application. In *AIP Conference Proceedings*, vol. 2009, no. 1, 020023 (AIP Publishing LLC, 2018).
28. Lamdhade, T., Raghuwanshi, G. C., Agrawal, F. M., Balkhande, R. M., Shripath, T. & V. and SnO_2 nanoparticles synthesis via liquid-phase co-precipitation technique. *Adv. Mater. Lett.* **6** (8), 738–742 (2015).
29. Siddique, M. N., Ali, T., Ahmed, A. & Tripathi, P. Enhanced electrical and thermal properties of pure and Ni substituted ZnO nanoparticles. *Nano-Struct. Nano-Objects*. **16**, 156–166 (2018).
30. Jayaram, P., Pradyumnan, P. P. & Karazhanov, S. Z. Micro-strain, dislocation density and surface chemical state analysis of multication thin films. *Phys. B Condens. Matter*. **501**, 140–145 (2016).
31. Gaur, J. et al. CTAB-crafted ZnO nanostructures for environmental remediation and pathogen control. *Sci. Rep.* **14** (1), 20561 (2024).
32. Nayman, E., Gozukizil, M. F., Armutci, B., Temel, S. & Gokmen, F. O. Structural and gas sensing properties of NiO thin films deposited by a novel spin coating technique. *J. Solgel Sci. Technol.* **114** (2), 386–398 (2025).
33. Mohammed, K. S., ALzanganawee, J. & Kamil, A. A. A novel approach to low-temperature gas sensing using sol–gel spin-coated (NiO:ZnO:SnO_2) thin films for NO_2, H_2S, and NH_3 detection. *J. Sol-Gel Sci. Technol.* 1–25 (2025).
34. Bolli, E. et al. Engineered SnO_2-based thin films for efficient CO_2 gas sensing at room temperature. *Appl. Surf. Sci.* **683**, 161795 (2025).
35. Haq, S. et al. Antibacterial, antioxidant and physicochemical investigations of Tin dioxide nanoparticles synthesized via microemulsion method. *Mater. Res. Express*. **8** (3), 035013 (2021).
36. Nasrallah, T. B., Mahboub, D., Jemai, M. & Belgacem, S. Temperature effect on Al/p-$CuInS_2$/SnO_2 (F) Schottky diodes. *Eng. Technol. Appl. Sci. Res.* **9** (5), 4695–4701 (2019).
37. Prabakaran, K. et al. Synthesis of zinc oxide and Tin oxide (ZnO/SnO_2) nanocomposite for photoanode applications in dye sensitized solar cell. *J. Mater. Sci. Mater. Electron.* **35**(30), 2024 (1993).
38. Zhang, J., Liu, X., Neri, G. & Pinna, N. Nanostructured materials for room-temperature gas sensors. *Adv. Mater.* **28** (5), 795–831 (2016).
39. Khan, L. A. et al. Investigation of the Fe-doped SnO_2 NPs with enhanced H_2S gas sensing performance. *Ceram. Int.* **51** (5), 6783–6792 (2025).
40. Gibson, N., Kuchenbecker, P., Rasmussen, K., Hodoroaba, V. D. & Rauscher, H. Volume-specific surface area by gas adsorption analysis with the BET method. In *Characterization of Nanoparticles*, 265–294 (Elsevier, 2020).
41. Du, M. et al. Enhanced selectivity electronic nose systems for agricultural ammonia gas detection via a co-designed WO_3-ZnO sensor array and convolutional neural networks. *Sci. Rep.* **15** (1), 39100 (2025).
42. Vasan, R., Gao, F., Manasreh, M. O. & Heyes, C. D. All-inorganic QLEDs utilizing resonant energy transfer between non-stoichiometric nickel oxide hole transport layer and alloyed CdSe/ZnS quantum Dots. *J. Mater. Sci. Mater. Electron.* **36** (19), 1190 (2025).
43. Wang, Y., Cui, Y., Meng, X., Zhang, Z. & Cao, J. A gas sensor based on Ag-modified ZnO flower-like microspheres: Temperature-modulated dual selectivity to CO and CH_4. *Surf. Interfaces*. **24**, 101110 (2021).
44. Song, W. et al. Ultraviolet photodetector based on p+-Si/n-ZnO bilayer structure. *Sci. Rep.* **15** (1), 37216 (2025).

45. Degler, D., Weimar, U. & Barsan, N. Current understanding of the fundamental mechanisms of doped and loaded semiconducting metal-oxide-based gas sensing materials. *ACS Sens.* **4** (9), 2228–2249 (2019).
46. Korotcenkov, G. *Handbook of Humidity Measurement, volume 1: Spectroscopic Methods of Humidity Measurement.* (CRC Press, 2018).
47. Bartolomé, J., Taeño, M., Martínez-Casado, R., Maestre, D. & Cremades, A. Ethanol gas sensing mechanisms of p-type NiO at room temperature. *Appl. Surf. Sci.* **579**, 152134 (2022).
48. Ahmed, S. & Sinha, S. K. Studies on nanomaterial-based p-type semiconductor gas sensors. *Environ. Sci. Pollut. Res.* **30** (10), 24975–24986 (2023).
49. Kim, H. J. & Lee, J. H. Highly sensitive and selective gas sensors using p-type oxide semiconductors: overview. *Sens. Actuators B* **1**(192), 607–627 (2014).
50. Wu, Q. et al. Hydrothermal synthesis of SnO_2-decorated Hollow ZnO nanospheres as sensing materials for CH_4 detection in power equipment oil. *J. Alloys Compd.* 185147 (2025).
51. Brunet, E. et al. Comparison of the gas sensing performance of SnO_2 thin film and SnO_2 nanowire sensors. *Sens. Actuators B.* **165** (1), 110–118 (2012).
52. Zou, C., Liang, F. & Xue, S. Synthesis and oxygen vacancy related NO_2 gas sensing properties of zno: Co nanorods arrays gown by a hydrothermal method. *Appl. Surf. Sci.* **353**, 1061–1069 (2015).
53. Farea, M. A. et al. Synergistic enhancement of CO gas sensing performance using SnO_2-Integrated polypyrrole/graphene oxide nanocomposites. *Mater. Sci. Semiconduct. Process.* **188**, 109219 (2025).
54. Park, J. et al. Formaldehyde gas response and selectivity of ZnO-SnO_2 gas sensors. *Sens. Actuators B.* **425**, 136958 (2025).
55. Chae, M. et al. Robust response to NO_2 gas on SnO_2 Heater/CNT gas sensor structures. *Sens. Actuators B Chem.* 138128 (2025).

Author contributions

P.C., K.S.: Conceptualization, methodology, software, visualization, investigation, writing-original draft preparation. R.K., T.Y.: Data curation, validation, supervision, resources, writing-review and editing. M.B., O.R.: Project administration, supervision, resources, writing-review and editing.

Funding

This work received no external funding.

Declarations

Competing interests

The authors declare no competing interests.

Additional information

Correspondence and requests for materials should be addressed to O.R.

Reprints and permissions information is available at www.nature.com/reprints.

Publisher's note Springer Nature remains neutral with regard to jurisdictional claims in published maps and institutional affiliations.